Numerical Simulation of the Aerodynamics and Acoustics of a Wall-Mounted Spoiler

Owen Parnis* and David Angland†
Faculty of Engineering and Physical Sciences,
University of Southampton, Southampton, SO16 7QF, United Kingdom.

A steep descent with deployed spoilers is a potential noise abatement procedure. This study investigates noise sources solely due to the spoiler by examining a spoiler mounted on a flat plate. An experimental database consisting of aerodynamic loads, microphone measurements, on-surface pressure distributions, hot wire anemometry, and particle image velocimetry is presented. Numerical simulations, performed using a Lattice Boltzmann solver ProLB, are validated against these experimental data. While the geometry is relatively simple, this is still a challenging case to accurately predict numerically, particularly the boundary layer separation bubble that occurs upstream of the spoiler. The flow is characterized by an arch-type broadband wake without any coherent vortex shedding. There is a horseshoe vortex that originates upstream of the spoiler and wraps around both sides of the spoiler. Inboard of the horseshoe vortex there are a pair of ground vortices with the opposite sign vorticity to the horseshoe vortex. A combination of band-filtered on-surface pressures and 3D numerical beamforming was used to determine the noise sources. As well as the broadband bluff body wake and the horseshoe vortex, the beamforming showed that the ground edge vortices and the spoiler side-edges were the dominant acoustic sources.

Nomenclature

a = speed of sound
b = span
C_D = drag coefficient
C_L = lift coefficient
C_p = pressure coefficient
c = chord of spoiler

---

*PhD Candidate, Aerodynamics and Flight Mechanics Group, Email: o.parnis@soton.ac.uk.
†Associate Professor, Airbus Noise Technology Centre, Email: d.angland@soton.ac.uk.
Presented as Paper 2024-3172 at the 30th AIAA/CEAS Aeroacoustics Conference (2024), June 4-7 2024, Rome Italy.

g = gap between the leading edge of the spoiler plate and the base plate

h = pitch correction

h_{domain} = height of fluid simulation domain

k = three dimensional turbulent kinetic energy

k_{yaw} = yaw correction

k_{2D} = two dimensional turbulent kinetic energy

k^* = wake height growth factor

L_{nozzle} = length of nozzle

l_{domain} = length of fluid simulation domain

p_{amb} = reference pressure

Re = Reynolds Number

S_{ref} = reference surface area

T = simulated time

t = thickness of spoiler plate

$|U|$ = velocity magnitude

U_∞ = freestream velocity

U_{eff} = effective cooling velocity

(u', v', w') = fluctuating velocity component

(u_{eff}') = fluctuating effective cooling velocity component

w_{domain} = width of fluid simulation domain

(x, y, z) = coordinate system

x_{LE} = distance from the wind tunnel origin along the x axis

z_{LE} = distance from the wind tunnel origin along the z axis

x^* = normalised x-axis with the chord of the flat plate spoiler

y^* = normalised y-axis with half the span of the flat plate spoiler

z^* = normalised z-axis with the chord of the flat plate spoiler

Δ = mesh size

ΔC_D = difference in the drag coefficient between numerical and experimental results

ΔC_L = difference in the lift coefficient between numerical and experimental results

Δt = numerical time step

Δx_{min} = minimum mesh size

δ = boundary layer thickness

δ_{sp} = spoiler deflection angle
θ = microphone polar angle
λ = wavelength of sound waves
ρ_{ref} = reference density
ω_{x} = vorticity about the x-axis
ω_{y} = vorticity about the y-axis
DRT = Dual Relaxation Time
FW-H = Ffowcs-Williams and Hawkings
LBM = Lattice Boltzmann Method
LES = Large Eddy Simulation
PIV = Particle Image Velocimetry
PSD = Power Spectral Density
SISM = Shear Improved Smagorinsky Model
SPL = Sound Pressure Levels
TKE = Turbulent Kinetic Energy

I. Introduction

The introduction of policies and regulations aimed at reducing the acoustic impact of air travel on communities, particularly during the approach to landing phase, has driven the study of steeper descent approach angles as a noise abatement procedure. These steeper angles, exceeding the conventional 3° glide slope angle, allow aircraft to commence their descent from higher altitudes above the ground during the approach phase [1]. This increase in altitude provides a greater propagation distance between the aircraft and the ground, thereby reducing community noise at ground level. However, steeper descent angles result in higher approach velocities during landing [2]. To ensure passenger comfort and in order to control the approach speed during the landing phase [3, 4], spoilers are deployed to slow down the aircraft so as to achieve the required rate of descent within the allowable vertical approach velocity specified.

Research has been conducted to analyze the flow field surrounding a high-lift wing equipped with a deployed spoiler during a steep descent and the resultant noise radiated to the far-field [5–7]. The flow topology of the deployed spoiler is characterized by an unsteady wake, akin to bluff bodies, whose wake width increases as a function of the spoiler deflection angle, δ_{sp}. The spoiler deflection changes the pressure distribution on the wing, influencing the flow field around the other high-lift devices. As also pointed out by Dobrzynski [4] and Kanjere et al. [7], the influence of a deflected spoiler induces changes to the wing's circulation, leading to variations in the slat and flap noise due to the changes of the circulation. Decoupling the noise generated by the spoiler itself from the high-lift wing noise hence becomes a difficult task.

In order to address this, a simplified flat plate model of a deflected flat plate spoiler mounted on a horizontal surface is studied (shown in Fig. 1). Using such a configuration, the spoiler's flow topology and noise sources can be assessed without the influence of changing the other high-lift device sources. The simplified geometry can be compared to three-dimensional, short aspect ratio, wall-mounted bodies, with potential applications extending beyond the aviation sector. This includes the energy sector, such as photovoltaic plates, and the automobile sector, for example in the design of deflector plates. The simplified setup presented in this work also provides an experimental database for numerical validation, which in spite of its relatively simple geometry, still contains some challenging aerodynamic phenomena to accurately capture in numerical simulations.

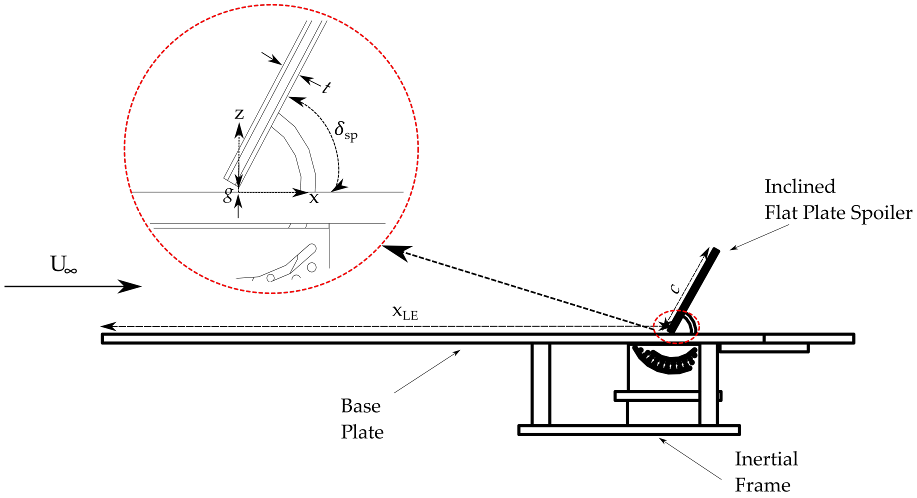

Fig. 1 Schematic of the inclined wall-mounted flat plate spoiler model.

The mean flow structure upstream of a wall-mounted flat plate exhibits similarities to the flow characteristics observed in the context of junction flows along wall-mounted bluff bodies, including plates [8–11], cylinders [12, 13] and prisms [14–16]. A wall-mounted body in the presence of a freestream flow induces a streamwise adverse pressure gradient upstream of the body. This adverse pressure gradient causes the boundary layer to separate upstream of the junction between the body and the wall. The formation of the resulting recirculation region depends on the Reynolds number and the boundary layer thickness [17, 18].

When a flat plate is mounted to a larger planar surface, such as the case in wall-mounted flows, the dominant influence of the mounting surface inhibits the occurrence of the vortex shedding phenomenon typically observed when the plate is in freestream flow [19]. This is primarily attributed to the planar mounting surface inhibiting the development of the shear layer with opposite sign vorticity that bounds the wake. Additionally, the aspect ratio of the plate's geometry plays a critical role in determining the nature of vortex separation downstream of wall-mounted bodies [13, 20]. As the aspect ratio of a mounted body is increased, the nature of the wake transforms from periodically shed, coherent Karman-type vortices at low aspect ratios to symmetric arch-type vortices [21].

Research on surface-mounted tabs [22–24], whose flow topology is analogous to inclined wall-mounted bodies on flat mounting surfaces, has suggested that for inclined-wall-mounted plates, the downstream flow topology contains three main vortex structures. First, a bluff body recirculatory region is observed immediately downstream of the plate. The plate's geometry influences the size of this recirculatory region and it increases with increasing deflection angle. Second, along the sides of the inclined plate, two contra-rotating vortex pairs form due to the pressure differences between the upstream and downstream faces of the plate. Third, hairpin vortices are formed due to the unstable shear layers along the trailing edges of the inclined plate. As these hairpin vortices convect downstream, they entrain fluid from the freestream, contributing to the expansion of the bluff body wake generated by the body.

While previous research has explored the flow topology of wall-mounted plates, there is still a significant gap in the understanding of the link between the flow features and their strength as acoustic sources. Most research is limited to geometries involving wall-mounted cylinders and prisms [25–28]. Parnis and Angland [29] extended this research to wall-mounted flat plate geometries, demonstrating that the acoustic noise generated by inclined wall-mounted flat plates at different flat plate deflection angles (corresponding to the deflection angle δ_{sp} in Fig 1) exhibits broadband characteristics which scaled broadly, but not perfectly, with the projected area of the plate and the sixth power of the freestream velocity. This implied that although the major noise sources were dipole in nature, as typically observed for wall-mounted bluff bodies, there were some additional mechanisms that contributed to the overall radiated noise source.

This paper has two primary aims. The first is to present an experimental database for a wall-mounted spoiler at a deflection angle of 30° that can be used for numerical validation. While the geometry is relatively simple, this is still a challenging case to accurately predict numerically, as will be discussed later. The second aim involves using this experimental database to validate a Lattice Boltzmann solver (ProLB) on this configuration. The validated numerical methodology is then used to investigate the flow topology and noise sources of a wall-mounted deflected spoiler. A deflection angle of 30° is chosen as this is representative of the deflection angle at which spoilers are deployed during flight. The advantage of having the spoiler mounted to a flat plate is that the flow topology and noise source analysis of a wall-mounted deflected spoiler can be performed in the absence of external influences from lifting bodies and any changes in circulation modifying other sources on a high-lift wing. While previous studies have explored simplified models as discussed above, this work aims to link the noise source with the specific flow features responsible to these noise sources on an isolated spoiler. It also presents a comprehensive aerodynamic and acoustic dataset, acquired in the same facility, that can be used for numerical validation. Firstly, the experimental and numerical methodologies are presented. The results are split into two main sections. Initially, the numerical simulations are validated with experimental results obtained for the same geometric configuration from experiments conducted in an anechoic wind tunnel. Following the numerical validation and a mesh dependency study, the numerical simulation results will be used to define the flow topology around the wall-mounted inclined spoiler and the corresponding noise source mechanism responsible for the radiated far-field noise.

II. Methodology

Numerical simulations were conducted in order to understand the main flow features of an inclined spoiler and how the on-surface pressure fluctuations induced by these flow features are radiated to the far-field as noise. To establish the validity of the numerical results, a comparison with experimental results was done for the same model configuration.

A. Experimental Approach

The experiments were conducted at the anechoic wind tunnel facility at the University of Southampton (SotonAWT). The tunnel is an open jet, closed return wind tunnel with a nozzle cross-section of 0.75 m by 1 m. In an empty test section, the maximum freestream velocity of the tunnel is approximately 80 m/s. The anechoic chamber is fitted with acoustic wedges and is anechoic down to a frequency of 250 Hz. These wind tunnel experiments were conducted at a freestream velocity of 60 m/s. The background noise level at 60 m/s was approximately 79 dBA measured at a reference point [30].*

The finite-span flat plate spoiler model was constructed from a thin steel plate with a chord of c = 106 mm and a span of b = 247 mm. The reference area used in the calculation of the force coefficients is S_{ref} = 0.026 m^2. The plate's aspect ratio is equal to 2.3. The plate's thickness is t = 6 mm. Additionally, no edge rounding was performed on the flat plate's sharp edges. The spoiler was deflected in the direction of the incoming flow stream using two brackets mounted on the downstream face of the plate at a spanwise location of $\pm 0.22\, b$ from the spoiler centreline.

A schematic representation of the flat plate model can be seen in Fig. 1, with the deflection angle δ_{sp} measured between the flat plate (deflected in the same direction as the freestream velocity vector) and the base mounting plate. The experiments were conducted at a free stream velocity of 60 m/s and a deflection angle of 30°, corresponding to a Reynolds Number of 4.5×10^5, calculated based on the chord length of the spoiler plate. The study was based on a deflection angle of 30°, as it is a representative angle at which spoilers are typically deployed during a steep descent. The model was securely mounted on a base plate attached to the lower lip of the wind tunnel nozzle, creating a three-quarters open test section. This configuration ensured quiescent flow underneath the base plate section. The model's origin was fixed at a specific location, with x_{LE} = 647 mm and z_{LE} = -375 mm measured with respect to the wind tunnel's origin, located at the centre of the wind tunnel nozzle exit.

A small gap was designed between the leading edge of the downstream face of the flat plate and the base plate. This was implemented to ensure the complete transfer of all aerodynamic loads acting on the flat plate to the load cell situated below the base plate. The gap size, denoted as g, between the leading edge and the base plate, varied with the deflection angle of the flat plate model, reaching a maximum gap ratio of g/c = 0.019. At the position of the spoiler's leading edge,

---

*The reference point was at a distance of 2.33 m from the centre of the nozzle exit at a polar angle of 120°.

the boundary layer thickness to gap ratio is represented as δ/g, equal to 14 and a boundary layer thickness to chord ratio (δ/c), equal to 0.26. The presence of the inclined spoiler plate introduces an adverse pressure gradient upstream of it, which varies with deflection angle. This adverse pressure gradient leads to the thickening of the boundary layer upstream of the flat plate. Consequently, the gap becomes significantly immersed within the boundary layer, where the velocities are significantly lower than the freestream velocity. No boundary layer tripping was done on the mounting plate.

Different experimental methodologies were used to generate an experimental data set of the flow characteristics and noise sources generated by the deflected spoiler to validate the numerical simulations. Aerodynamic loads on the model were measured using an ATI Delta 6-component transducer connected to the inertial frame of the wind tunnel. The drag and lift forces are aligned along the model's positive x and z axis, respectively, as shown in Fig. 1. Measurements were taken at a sampling rate of 1 kHz for a total of 30 seconds. The dynamic pressure used in the calculations of the force coefficients was a Furness controls FCO332-4W differential pressure transducer, and the uncertainty was less than ±0.5% of the reading. The freestream dynamic pressure in the test section was determined using the pressure differential between two static ring measurements in the nozzle contraction. This pressure differential has been calibrated to give the dynamic pressure at 0.5 m downstream of the nozzle exit [30]. The final uncertainty values of the force coefficient values, including both Type A and Type B uncertainties, are included in the presentation of the force results [31].

Acoustic measurements were conducted using a total of thirteen GRAS 1/4" 46BE microphones. The microphones were set up as shown in Fig. 2. Seven microphones were set up along $y = 0$ m (corresponding to the mid-span of the model) above the spoiler for polar angles between 70° and 101°. The vertical distance (z) between the model's coordinate system specified in Fig. 1 and the overhead microphones was approximately $z = 1.33$ m. The physical locations of the microphones with respect to the model coordinate axis specified in Fig. 1 are provided in Appendix A in Table A.1. Microphone measurements were taken at a sampling frequency of 25.6 kHz for a total sampling time of 31 s. The results presented in this study for numerical validation will only consider three overhead arc microphone locations along the plane of symmetry of the model at $\theta = 76°$, 90° and 101°. In spite of such a small spoiler model (ratio of spoiler frontal area, at a deflection angle of 30°, to the wind tunnel nozzle cross sectional area was only 1.75%), the signal to noise ratio over the background noise of the facility was 3 dB or greater for each of the three microphone locations from octave band frequencies of 125 Hz to 2 kHz. At an octave band of 4 kHz and above, where the spoiler noise was no longer dominant, the signal to noise ratio reduced to approximately 2 dB.

On-surface measurements were done using 34 pressure taps along the base plate and the upstream and downstream faces of the inclined flat plate. The surface measurements on the model were measured using a ZOC33/64PX (Operate, Calibrate, Purge and Isolate) pressure scanner system from Scanivalve Ltd. The system comprises 64 individual piezo resistive pressure sensors capable of reaching a scan rate of 40 kHz. The uncertainty was ±0.15% for the full-scale values. The location of the pressure taps on the model with respect to the model coordinate system shown in Fig. 1 are presented in Appendix A in Table A.2. Figure A.1 shows a schematic of the pressure tap locations on the model.

Fig. 2 Experimental setup showing the location of the microphones.

The upstream boundary layer characteristics were determined using a total pressure Preston tube mounted on a three-dimensional traverse system. The boundary layer velocity profile was derived from dynamic pressure measurements, calculated from the total pressure readings from the Preston tube readings and the interpolated static pressure field from the streamwise pressure taps on the model centreline and assuming zero pressure gradient normal to the wall. The near wake downstream of the flat plate was characterized using hotwire anemometry and two-dimensional Particle Image Velocimetry (PIV) measurements. A schematic of the wake characteristics measurements conducted is provided in Fig. 3.

The wake characteristics were measured using hotwire measurements. A single-probe hotwire (DANTEC wire probe type 55P16) was used to analyze the turbulent wake downstream of the plate. The probe was mounted on a three-dimensional automated traverse system and connected to a DANTEC MiniCTA 54T30 anemometer. Measurements were obtained at two distinct streamwise locations downstream of the inclined plate. The distances are equivalent to $\mathrm{HW}_1 = 1.5c$, and $\mathrm{HW}_2 = 2c$ from the leading edge of the model, where c represents the chord of the flat plate model. These measurements followed a grid that spanned the entire span of the flat plate while extending beyond the edges of the flat plate to allow for the growth of the downstream wake. The results yielded a spanwise crosswind representation of the velocity mapping and the regions of turbulence in the wake for different streamwise positions downstream of the flat plate. The data acquisition was performed using a National Instruments NI-4497 card at a frequency of 48 kHz, with a sampling time of 10 s. A fourth order polynominal was used for the calibration. The maximum uncertainty in the velocity measurements was ±0.8 m/s and in the turbulent intensity was ±2.68% at 60 m/s.

The streamwise characterization and wake growth of the wake downstream of the inclined flat plate were determined using 2D Particle Image Velocimetry (PIV). Velocity vectors in the streamwise and vertical (z-axis) directions were

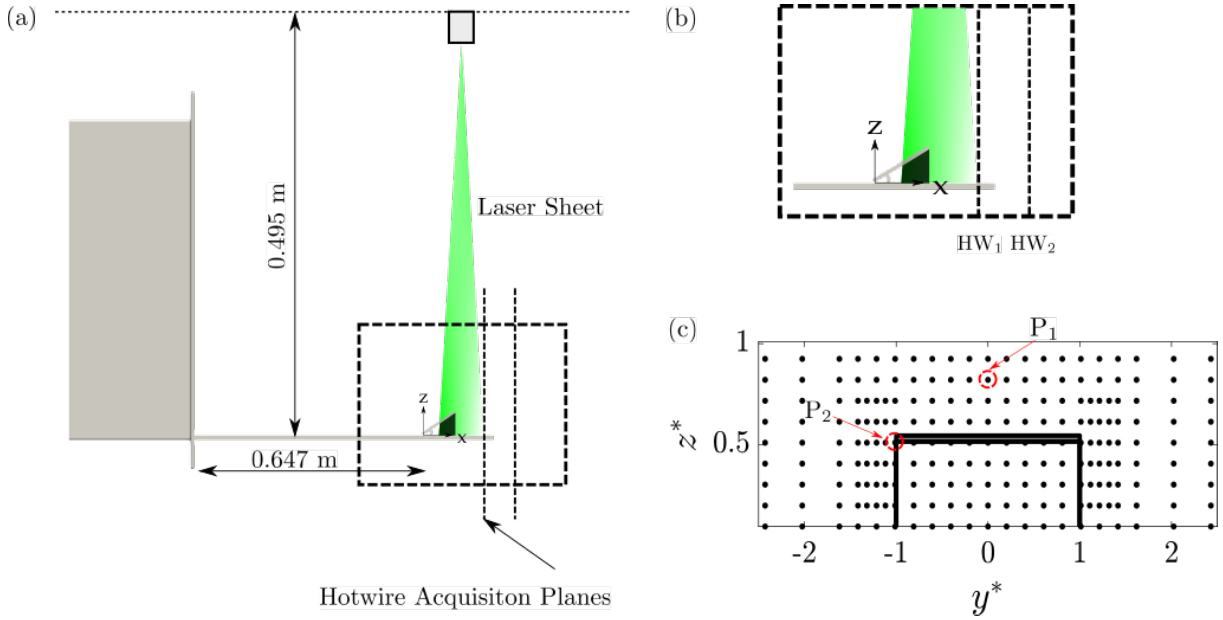

Fig. 3 Experimental setup: (a) PIV configuration to capture the streamwise symmetry plane, (b) hotwire measurement locations, and (c) hotwire array points for wake mapping.

measured along the symmetry axis of the model (y = 0 mm). A laser sheet was generated above the model and illuminated the near downstream region of the mounted plate. Images were captured using a 25 MP LaVision Imager CX series camera with a maximum resolution of 5296 × 4584 pixels and a frame rate of up to 30.4 Hz. The images were acquired at an acquisition frequency between 4.5 Hz and 9 Hz. Oil-based smoke seeding was generated using a Martin Magnum 1200 smoke generator. One thousand dual-frame image pairs were acquired. Image pre-processing was done by applying a sliding subtraction of the minimum intensity calculated from a filter length of 49 images. Vector calculation was done using multi-pass interrogation windows, with the final pass having an interrogation window size of 64 × 64 pixels with an overlap of 75%.

B. Numerical Approach

The flow topology and noise sources are analysed using numerical simulations performed using ProLB, a numerical solver based on the Lattice Boltzmann equations. ProLB 2.6.3 DC was used for all of the simulations presented in this paper. The solver employs a Lattice Boltzmann Method (LBM) kernel using a D3Q19-lattice scheme with a dual relaxation time (DRT) collision operator, as defined by Leveque et al. [32]. ProLB incorporates a fully parallel, inbuilt octree mesh generator.

Unsteady simulations for turbulent flow were conducted using wall-modelled large eddy simulations (LES), employing a subgrid-scale model based on the shear-improved Smagorinsky model (SISM). The wall law was modelled using a log-law with adverse pressure gradient terms and curvature corrections, following the formulation proposed by Afzal [33] and Patel and Sotiropoulos [34].

1. Numerical Setup

The numerical results were validated against the experimental results for the same configuration and deflection angle. The open jet wind tunnel set-up in the anechoic chamber is simulated numerically. A straight wind tunnel duct was used to model the open jet in the wind tunnel and made the boundary conditions simpler to specify. It still replicated the open jet expansion and the formation of the shear layers along the nozzle exit, similar to the experiments. The duct length of the nozzle section is equal to 1.8 m, and the nozzle's cross-section area is equal to that of SotonAWT. A velocity inlet boundary condition set equal to the freestream velocity (U_∞) at the beginning of the straight duct. The model was fixed to the lower lip of the nozzle of the straight wind tunnel duct similar to the experiments. The leading edge of the spoiler is at a distance of 0.647 m from the nozzle exit. Fig. 4 shows a schematic of the simulation domain along the symmetry plane of the model (y = 0 m).

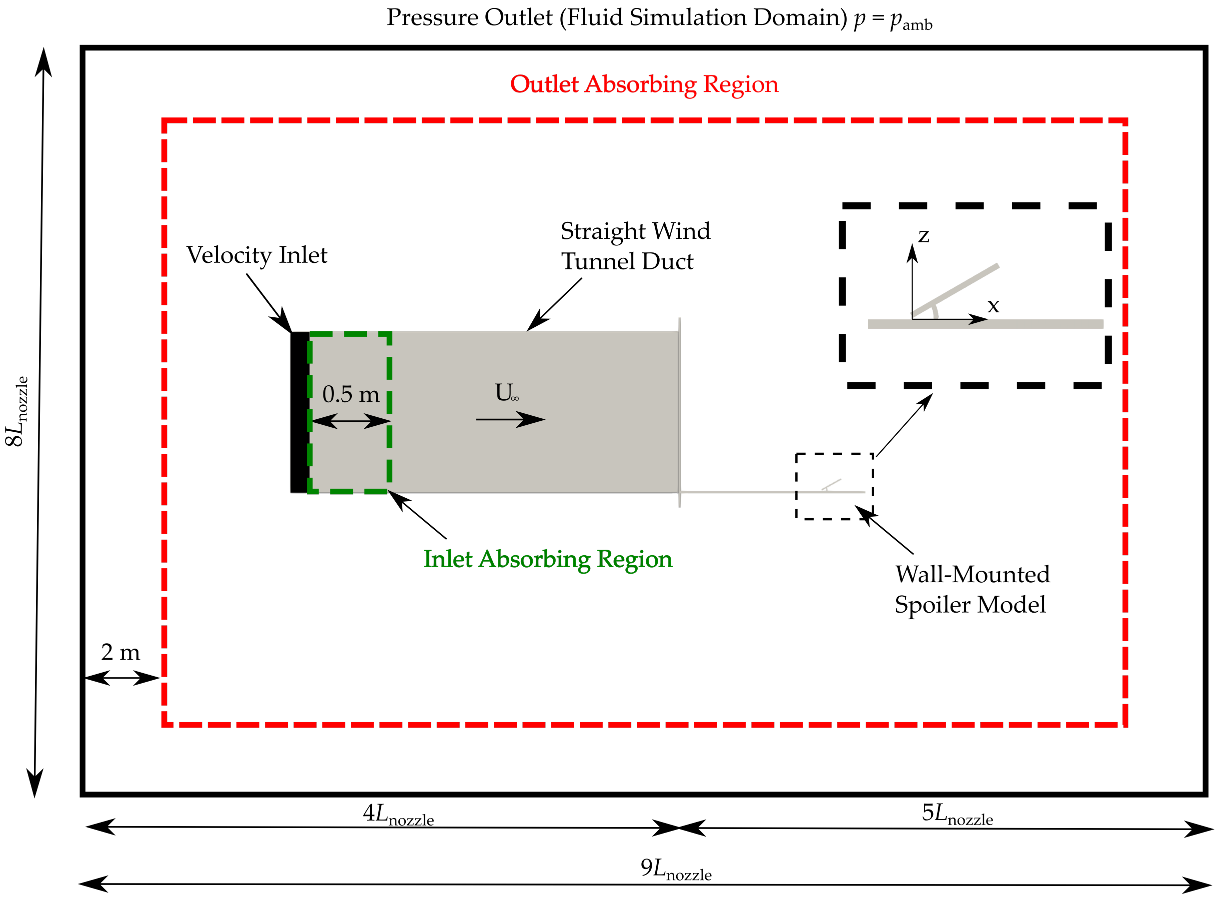

Fig. 4 Schematic of the simulation domain along the symmetry plane at y = 0 m. N.B. image is not to scale.

The dimensions of the fluid simulation domain is equivalent $l_{\text{domain}} = 9L_{\text{nozzle}}$, $h_{\text{domain}} = 8L_{\text{nozzle}}$, $w_{\text{domain}} = 8L_{\text{nozzle}}$, where L_{nozzle} is equal to the width of the nozzle outlet. A pressure outlet boundary condition was set at the fluid domain with the pressure equal to the ambient pressure, p_{amb}. To reduce spurious far-field reflections of the propagating acoustic waves from the edge of the computational fluid domain, an absorbing region with a thickness of 2 m was modelled. The thickness was selected to allow enough mesh points within the absorbing region for sufficient acoustic damping. An inlet absorbing region with a thickness of 0.5 m was also implemented at the beginning of the inlet nozzle. This prevented the development of any duct modes in the straight inlet nozzle and to prevent any reflections from the beginning of the inlet duct. The incoming flow is uniform with a freestream velocity of $U_\infty = 60$ m/s, temperature of $T = 288$ K and density of $\rho = 1.23$ kg/m^3. The equivalent speed of sound was equal to $a = 340.17$ m/s, resulting in a reference Mach Number, Ma = 0.18. A no-slip wall boundary condition was specified for the wall-mounted model and the nozzle duct. Similar to the experimental setup, no boundary layer tripping was modelled along the base mounting plate.

It is important to note that the wind tunnel collector and diffuser was omitted from the simulation to avoid difficulties in specifying the correct pressure outlet boundary conditions within the diffusing section of the wind tunnel with the spoiler model upstream. While this simplification enables a simplified numerical setup, and inlet and outlet boundary condition specification, it is clearly an approximation and excludes some aerodynamic and acoustic effects that are present in the experiments.

2. *Numerical Mesh*

The initial on-surface mesh size was set to $\Delta x_{\mathrm{min}} = 0.25$ mm. Subsequent refinement was done along the near-field downstream wake of the deflected plate up to a distance of $5c$, resulting in a total mesh size of $359{\times}10^6$ cells, corresponding to the fine mesh defined in Table 2. The mesh levels were selected to ensure the presence of at least eight mesh points per wavelength in regions of direct noise propagation, allowing for a maximum resolvable frequency of 10.6 kHz. This setup led to a minimum numerical time step $\Delta t = 4.24 \times 10^{-7}$ s. The total simulated physical time for this numerical analysis was equal to 0.307 seconds. This is equivalent to a convection time of $18.42(L_{\mathrm{nozzle}}/U_\infty)$. The mesh setup is shown in Fig. 5a.

Acoustic analysis was done using a Ffowcs Williams and Hawkings (FW-H) solver based on the Farassat 1A formulations [35]. Both porous and solid FW-H surfaces were used. The porous surface enclosed the spoiler and the adjacent base plate region (as shown in Fig. 5a). The porous surface was implemented as a cuboid. The coordinates of the cuboid are defined in Table A.4 relative to the coordinate system shown in Fig. 1. The surface dimensions of the porous FW-H surface were sufficiently large to ensure that no vorticity generated by the spoiler convects through the faces of the porous FW-H surface. The most downstream face of the porous integral surface was also excluded from the final FW-H calculation to avoid the vorticity in the wake convecting through this face of the integral surface. A refinement of $\Delta = 4$ mm was defined within and on the porous integration surfaces, allowing for a maximum resolvable frequency of approximately 10.5 kHz for acoustic waves.

Figure 5b, defines the volumetric refinement zones around the solid surfaces. To reproduce the experimental setup, a hinge gap was modelled between the leading edge of the spoiler and the mounting plate. Local refinement along the hinge gap, equal to the minimum mesh size, was done to ensure that enough internal fluid nodes were present between

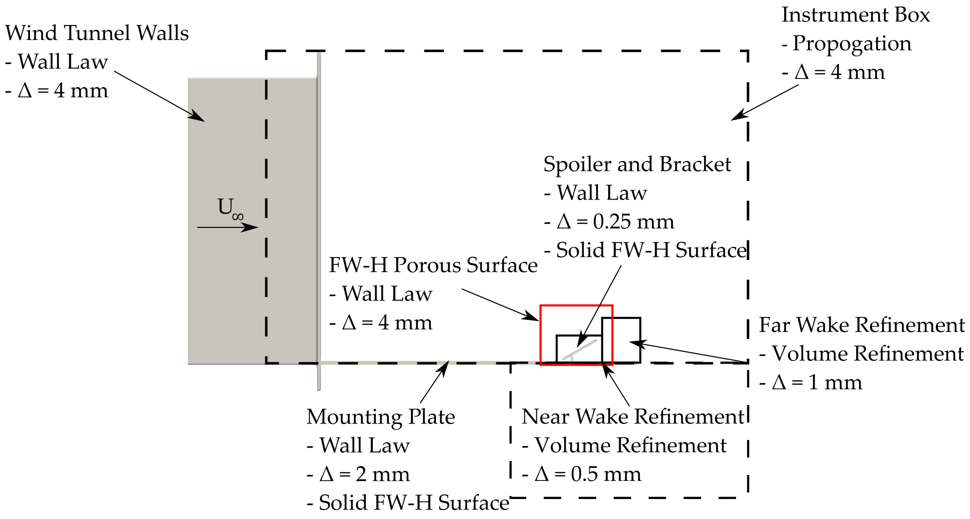

(a) Numerical Simulation Setup.

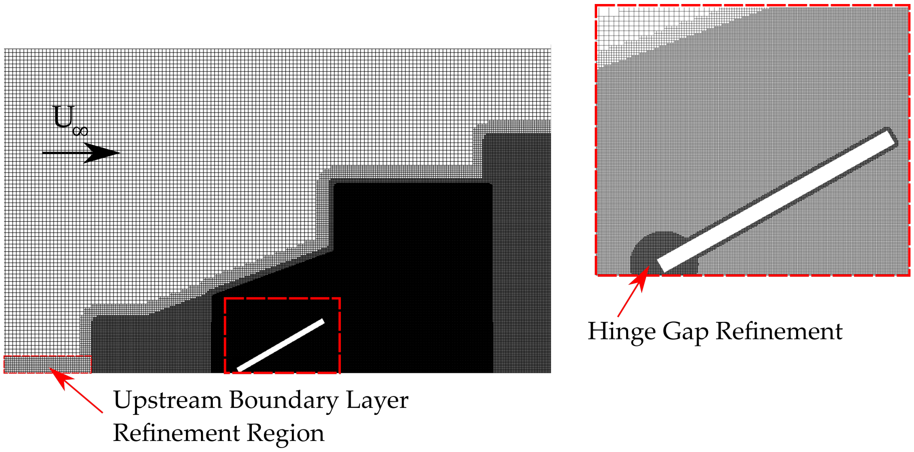

(b) Mesh refinement zones along the spoiler including the hinge gap refinement and boundary layer refinement region.

Fig. 5 Mesh setup and sizing.

the two surfaces to resolve correctly the flow emanating through the hinge gap. Along the mounting plate, upstream of the spoiler, a local refinement of $\Delta = 2$ mm was done to ensure that the local y^+ along the surface lies within the log-law region for wall-modelled boundary layers. This resulted in a maximum $y^+ = 260$ upstream of the inclined plate. Refining the surface to achieve a lower y^+ was found to be counterproductive as the agreement with experimental boundary layer profiles was worse (this is discussed later). A summary of the simulation parameters is presented in Table 1.

Feature	Condition
Turbulence Model	Wall modelled LES with Shear Improved Smagorinsky Model
Minimum Mesh Size	Δx_{min} = 0.25 mm
Mesh Size	359×10^6
Simulated Time	T = 0.307 s
Time step	$\Delta t = 4.24 \times 10^{-7}$ s
Speed of Sound	a = 340.17 m/s
Reference Pressure	$p_{\text{amb}} = 1.012 \times 10^5$ Pa
Reference Density	$\rho_{\text{ref}} = 1.23$ kg/m^3
Freestream Velocity	U_∞ = 60 m/s

Table 1 Summary of the numerical simulation setup conducted in ProLB.

III. Mesh Dependency

The influence of mesh resolution was examined by assessing the aerodynamic loads and far-field acoustics for a wall-mounted spoiler at a deflection angle of 30°. The results obtained from ProLB were compared to experiments conducted for the same configuration. A summary of the results is provided in Table 2. The surface mesh resolution on the mounting base plate and spoiler remained consistent across all configurations in order to keep the wall y^+ values constant. The mesh sensitivity was evaluated through progressive refinement of the volumetric mesh refinements in both the near-wake and far-wake regions shown in Fig. 5a. The reference area used in the calculation of the force coefficients is $S_{\text{ref}} = 0.026$ m^2.

Configuration	Mesh Size	Resources [core hours]	C_D	C_L	C_D error	C_L error
Experiment	-	-	0.221 ± 0.014	-0.333 ± 0.026	-	-
Coarse Mesh	73×10^6	2.3×10^5	0.247	-0.401	11.8%	20.4%
Medium Mesh	109×10^6	2.7×10^5	0.239	-0.384	8.1%	15.4%
Fine Mesh	359×10^6	9.5×10^5	0.233	-0.374	5.4%	12.3%

Table 2 Summary of the mesh resolution study for aerodynamic loads.

Figures 6a and 6b show a comparison of the aerodynamic loads simulated to the experimental results. For all the meshes examined, ProLB overpredicts both the drag and the lift coefficients, with larger discrepancies observed for the lift coefficient. Improvement in the aerodynamic coefficients was obtained by increasing mesh size with a reduction of the ΔC_D and ΔC_L between subsequent meshes. The best agreement was observed for the fine mesh in which the drag was overpredicted by 5.4%, and the lift was overpredicted by 12.3% when compared to the experimental results as shown in Table 2. Only small changes were seen in the aerodynamic coefficients between the medium mesh and the fine mesh. However, this came at a cost of more than triple the amount of computational resources used.

Figures 7a and 7c show the far-field spectra from both porous and solid FW-H surfaces for a microphone located at a

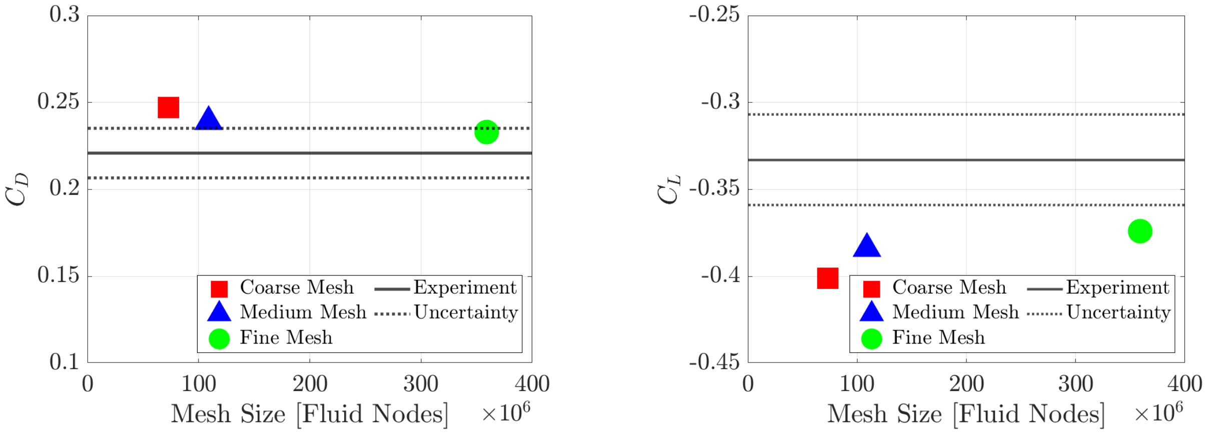

(a) Drag Coefficient.

(b) Lift Coefficient.

Fig. 6 Influence of mesh resolution on aerodynamic loads .

polar angle of $\theta = 90°$ above the leading edge of the spoiler compared to the experimental results. An increase in the mesh refinement resulted in better agreement with the experimental results for both the porous and solid FW-H surfaces, with the best agreement observed within 1 dB for both the medium mesh and the fine mesh for frequencies above 1 kHz for the porous FW-H. Underprediction of the noise generated at low frequency for the porous surface was due to the fact that the porous surface only encloses a small section of the base mounting plate.

Additionally, the spurious tonal peaks at 4 kHz and 8 kHz were attenuated with mesh refinement for both the porous and solid FW-H surfaces, as shown in Fig. 7b and Fig. 7d. These peaks were due to regions of under-refinement downstream of the hinge gap of the wall-mounted spoiler plate. These tonal peaks are observed to be removed by the fine mesh, providing the best agreement with the experiment among the meshes for both the porous surface and the solid surface.

Both the medium and the fine mesh compare well with experimental results. Convergence in the aerodynamic forces is observed between the medium and fine mesh. However, in terms of the acoustic spectra, the fine mesh shows small but measurable improvements in the far-field integrated spectra, particularly above 4 kHz. Hence, the fine mesh was selected to be used for further validation of ProLB.

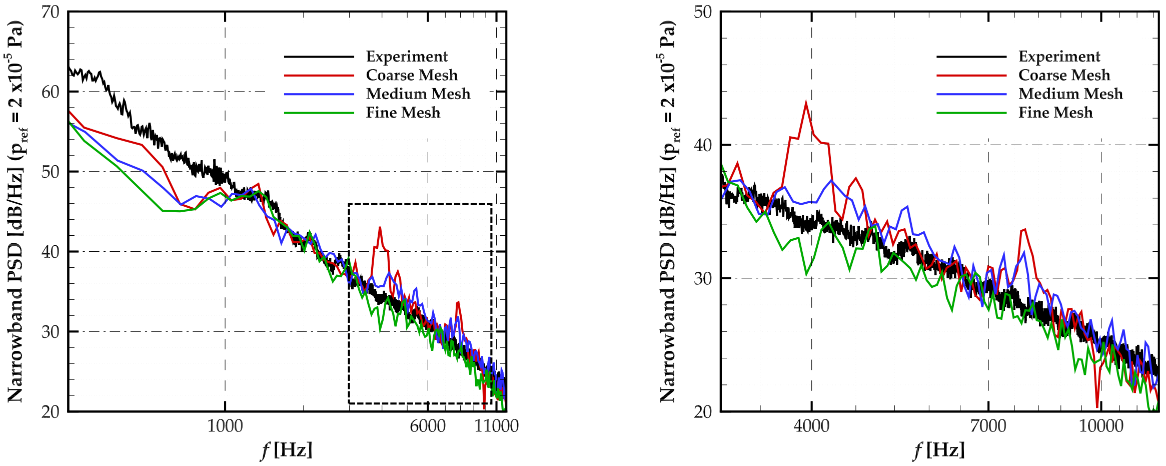

(a) Far-field spectra computed with FW-H porous surface data.

(b) Close up of spectra between 4 kHz and 11 kHz computed with FW-H porous surface data.

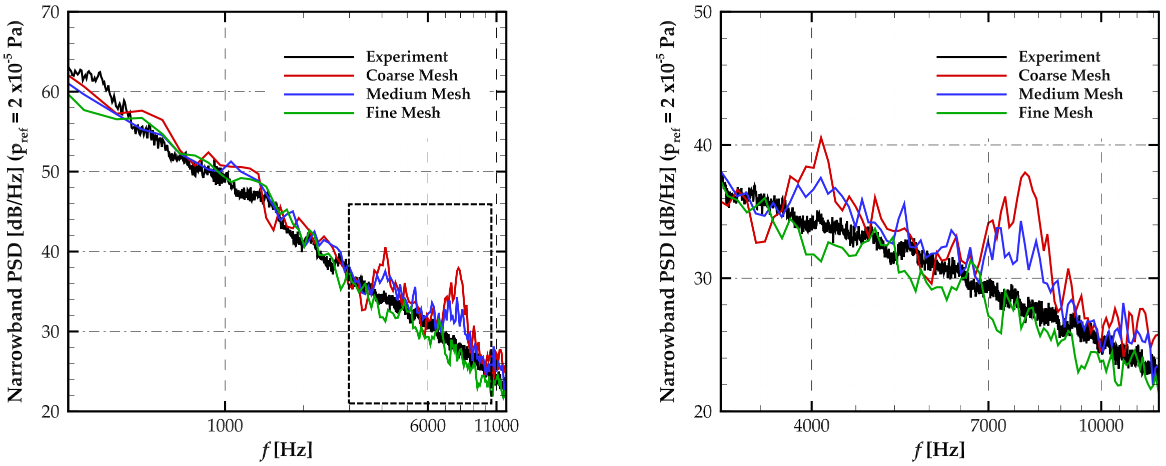

(c) Far-field spectra computed with FW-H solid surface data.

(d) Close up of spectra between 4 kHz and 11 kHz computed with FW-H solid surface data.

Fig. 7 Influence of mesh resolution on the far-field spectra from both porous and solid FW-H surfaces compared to experimental results at a polar angle of θ = 90°.

IV. Numerical Simulation Validation with Experimental Results

The numerical simulations are validated with experimental results obtained at a spoiler deflection angle of 30°. The validation encompassed a detailed comparison of numerical and experimental results, covering aerodynamic loads, far-field noise spectra, upstream boundary layer characteristics, on-surface pressures, and comparisons of wake characteristics.

A. Normalised Axis

Normalization of the coordinate axis was done with respect to the characteristic lengths of the spoiler plate and is applied to scale the axis relative to the characteristic lengths of the inclined spoiler. The equations of the normalized lengths x^*, y^* and z^* are shown in Eq. (1) to Eq. (3). To simplify the reference location of the different flow features with respect to the inclined spoiler plate, the origin of the axis was placed on the symmetry plane of the hinge axis of the spoiler. The coordinate system was previously shown in Fig. 4.

$$x^* = x/c \tag{1}$$

$$y^* = 2y/b \tag{2}$$

$$z^* = z/c \tag{3}$$

B. Aerodynamic Load Coefficients

A comparison of the simulated aerodynamic load coefficients with the experimental data was previously presented in Table 2. The deflected spoiler produces downforce (negative lift) and drag. As shown previously, the simulations with the fine mesh overpredict the experimental values for the drag coefficient and lift coefficient by ΔC_D = 5.4% and ΔC_L = 12.3%, respectively. The reasons for the discrepancy can be examined by looking at the on-surface pressure distributions.

C. Upstream Boundary Layer

The pressure distribution on the spoiler is dependent on the condition of the flow upstream of the spoiler's leading edge. As discussed earlier, the numerical setup included a straight wind tunnel nozzle to simulate the open jet wind tunnel. A boundary layer grows on the base plate upstream of the spoiler. The upstream boundary layer plays a crucial role in characterising the static pressure along both the base mounting plate and the inclined spoiler plate.

To assess the flow conditions upstream of the spoiler, mean velocity profiles were analyzed along the boundary layer at x^* = -4.4 and x^* = -3. These locations were chosen to be downstream of the accelerating flow of the wind tunnel nozzle. The results are shown in Fig. 8a and Fig. 8b.

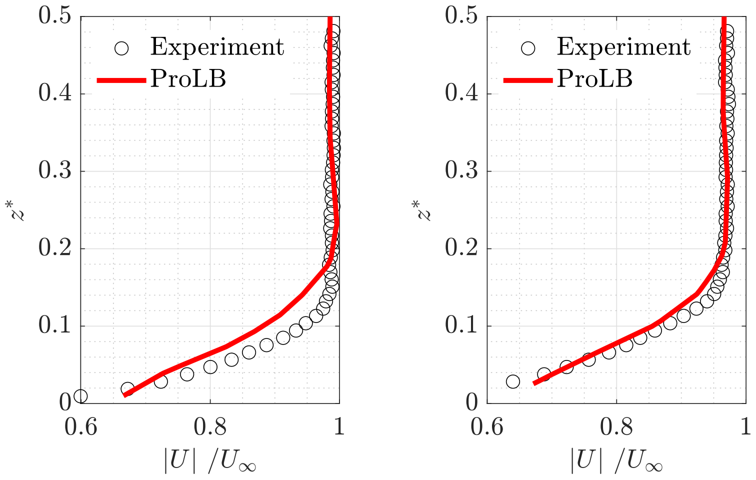

(a) x^* = -4.4

(b) x^* = -3

Fig. 8 Comparison of the boundary layer velocity profile between experimental and ProLB results at two streamwise locations upstream of the spoiler: (a) x^* = -4.4 and (b) x^* = -3.

The results obtained show that the wall-modelled LES model with the shear-improved Smagorinsky model used in ProLB is shown to predict a less developed velocity profile when compared to the experimental results at $x^* = -4.4$. In the experiments, the boundary layer had a measured power law exponent of 5.2. This is less than the power law exponent value for a fully developed turbulent boundary layer due to length of the mounting plate and the presence of the adverse pressure gradient due to the spoiler. Closer to the spoiler, a better prediction is observed at $x^* = -3$. Further refinement of the surface mesh and reducing the wall y^+ did not result in better agreement with the experimental data but, in general, led to a fuller turbulent boundary layer profile than was measured in the experiment.

D. Mean On-surface Pressure

The mean on-surface pressure was calculated along the symmetry plane (y = 0 m) along the base plate and the spoiler. The comparison of the coefficient of pressure plots is provided in Fig. 9. The numerical simulations are observed to underestimate slightly the on-surface pressure up to a distance of x^* = -2. The main reason for this difference is the disagreement in the upstream boundary layer properties previously discussed. Better agreement is observed along the region of pressure increase due to the adverse pressure gradient along the base plate until x^* = -0.67, where the onset of flow separation is predicted for both methodologies. Downstream of this, there is a disagreement in the pressure drop due to the separation upstream of the spoiler hinge and its streamwise extent. In both methodologies, there is separation and subsequent recirculation region forming at x^* = -0.57 (this is related to the formation of a horseshoe vortex that will be discussed later). Reattachment occurs along the upstream face of the spoiler, shortly after the leading edge. The numerical results predict the pressure drop corresponding to the separation and the horseshoe vortex occurring closer to the spoiler hinge line. This boundary layer separation bubble in the presence of an adverse pressure gradient is a very challenging flow feature to capture correctly numerically.

Due to the different locations of the flow separation and attachment, the pressure on the upstream face of the spoiler plate is overpredicted slightly compared to the experimental result, explaining the small variations in the aerodynamic coefficients previously presented. Downstream of the spoiler, it is observed that both the experiments and ProLB results predict similar levels of base pressure along the downstream face of the spoiler and the base plate within the recirculation region of the wake.

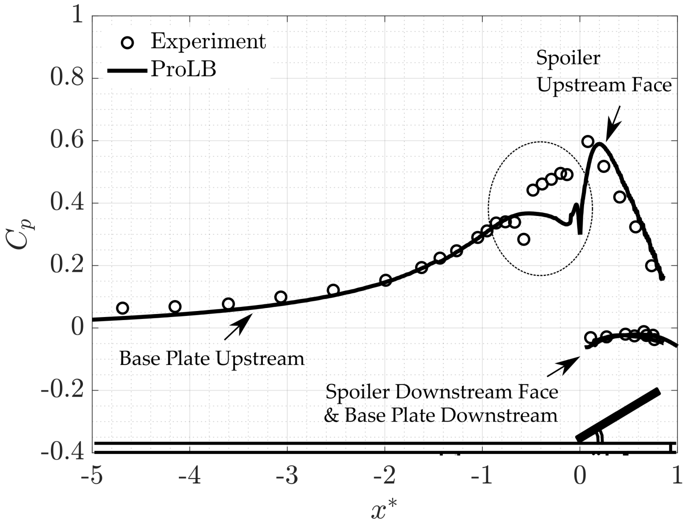

Fig. 9 Streamwise on-surface mean pressure distribution comparison between experimental results and ProLB on the different surfaces of the model.

E. Far-field Acoustics

The far-field noise radiated from the model was calculated using both solid and porous FW-H surfaces. The results were compared to microphone measurements at different polar angles (θ = 76°, 90° and 101°) above the spoiler. Figure 10 shows a comparison of the far-field noise radiated from the model, done by comparing the individual narrowband spectra calculated from both the porous and solid FW-H surfaces modelled. To examine the directivity of the radiated acoustic waves, the spectrum from three overhead locations was analysed.

In general, for the forward arc and the overhead arc, excellent agreement between the experimental results and the solid FW-H surface for the entire model (comprising of the spoiler plate, brackets and mounting plate) was observed for frequencies above 630 Hz, with the porous surface giving better agreement than the solid FW-H surface at frequencies above 1 kHz. This is not the case at lower frequencies. To understand why, Fig. 10 also shows the contribution of the pressure fluctuations on the deflected spoiler plate alone. The noise, due to pressure fluctuation on the spoiler surface alone, is observed to peak at a frequency of 1.25 kHz. At lower frequencies, the noise generated by the pressure fluctuations on the mounting plate dominates the far-field noise. It should be noted that the pressure fluctuations on the mounting base plate are not only a result of the unsteady flow generated by the presence of the spoiler but also, at low frequencies, the interaction of the open jet wind tunnel shear layers with the mounting plate. The porous FW-H surface contains the spoiler and the wake it generates, but only a portion of the mounting plate is contained within the porous integral surface. Also, the most downstream face of the integral surface is removed when performing the FW-H calculation to avoid vorticity in the wake of the spoiler convecting through this integral surface. These two effects are hypothesised to explain the discrepancy between the porous and solid FW-H results at low frequencies.

The far-field acoustics show that the noise generated by a deflected spoiler is broadband and without coherent tonal noise related to the mechanism of vortex shedding in the spoiler's wake or trailing edge. The small hinge gap discussed previously, is not a significant source of noise at this deflection angle of $\delta_{sp} = 30^\circ$. This was determined both experimentally and numerically by closing the gap. Only small differences below 1 kHz were found (data omitted here for brevity) in the spectra. N.B. this conclusion is only true of this deflection angle. At other deflection angles (only $\delta_{sp} = 30^\circ$ data presented in this paper) this was not always true and the hinge gap noise was measurable.

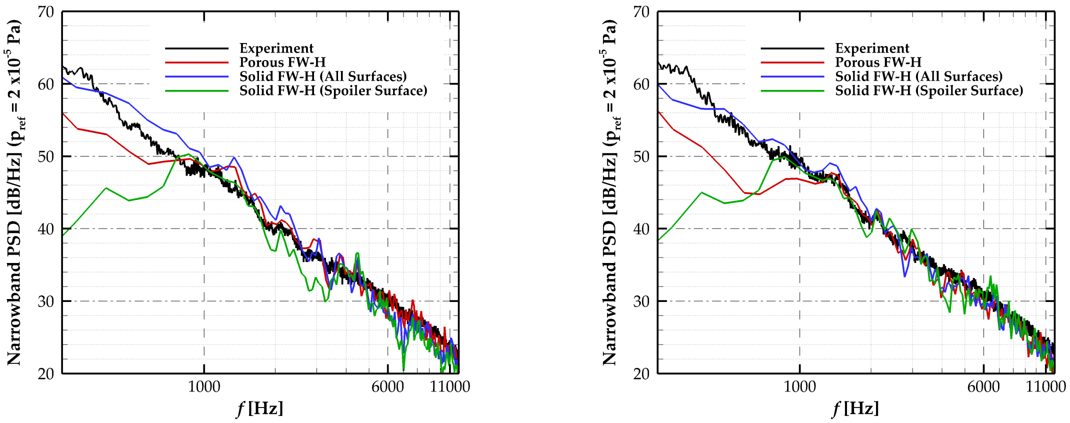

(a) Forward Arc: θ = 76°.

(b) Overhead: θ = 90°.

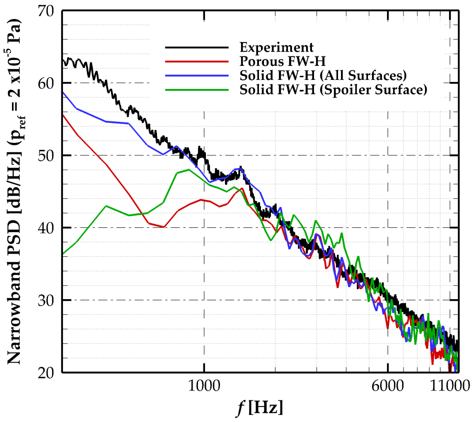

(c) Rearward Arc: θ = 101°.

Fig. 10 Comparison of the narrowband acoustic far-field spectra at three overhead locations: (a) θ = 76°, (b) θ = 90°, (c) θ = 101°.

F. Wake Characteristics

The wake characteristics and the turbulent fluctuations predicted by ProLB were validated against sampled data obtained from both hotwire anemometry and two-dimensional PIV measurements.

1. Single Point Turbulence Measurements

Single-point turbulence measurements in the wake were done by comparing the power spectral density (PSD) of the velocity fluctuations in different regions in the wake. The comparison was done with respect to the velocity fluctuations of the effective cooling velocity, u'_{eff} (defined in Eq. (4)) of the incoming flow [36]. The effective cooling velocity, U_{eff} (defined in Eq. (5)) takes into account the directional sensitivity of a single component hotwire probe in terms of pitch and yaw angle of the instantaneous velocity component of the incoming flow. The instantaneous velocity vector continuously changes its direction in a turbulent flow and therefore is not always perpendicular to the hot wire. The effective film cooling rates induced by the flow on the hotwire are a function of the direction of the velocity vector [37].

$$u'_{\mathrm{eff}} = U_{\mathrm{eff}} - \overline{U}_{\mathrm{eff}} \quad , \tag{4}$$

$$U^2_{\mathrm{eff}} = U^2_x + k^2_{\mathrm{yaw}} U^2_y + h^2 U^2_z \quad , \tag{5}$$

where U_{x} is the normal velocity component to the probe along the x-axis, U_{z} is the binormal velocity component to the probe along the z-axis, U_{y} is the tangential velocity along the length of the wire along the y-axis. The variable h is the pitch correction factor for the binormal velocity vector introduced to compensate for the acceleration of the flow over the wire due to the presence of the side prongs, and k_{yaw} is the yaw correction factor along the tangential velocity to correct for the increase in heat transfer rate along the wire due to the tangential component of the incoming flow. The correction factor values depend on the hotwire probe type, freestream velocity and yaw angle. For a miniature single probe, a value of $k_{\mathrm{yaw}} = 0.2$ and $h = 1.1$ are used [38]. Using this definition, the numerical three-dimensional instantaneous velocity vector, as established by a probe in the fluid simulation domain, is analysed in the same way as a three-dimensional flow experienced by a single hotwire probe in the experiments [39].

Analysis of velocity perturbations was done at two spanwise locations highlighted in Fig. 3c. Point P_1 is located downstream in the shear layer that grows from the trailing-edge of the spoiler. Point P_2 is located downstream, directly behind the intersection of the side and trailing-edge of the spoiler, as shown in Fig. 3c. The location of the two acquisition points with respect to the model's coordinate system is specified in the Appendix in Table A.3. Analysis of the power spectral density (PSD) for each point was done using Welch's method [40]. The reference velocity was taken as equal to the freestream velocity, $U_\infty = 60$ m/s. The results for the two acquisition planes are provided in Fig. 11.

Both numerical and experimental data show the development of broadband spectra in the wake without any coherent vortex shedding, confirming the conclusion obtained from the far-field acoustic data. Higher velocity perturbations are observed along the free shear layer generated from the trailing edge of the spoiler when compared to the perturbations along the shear layer generated from the side-edge. As the spoiler is placed in proximity to the base plate, the formation of a shear layer of opposite sign vorticity is inhibited. Hence, coherent von-Karman-type vortex shedding downstream of the spoiler plate is suppressed. Similarly, due to the aspect ratio of the spoiler plate, vortex roll-up between the two free side-edges is also suppressed due to the formation of symmetric arch-type vortices downstream of the plate [20, 21].

The turbulence spectra along the free shear layer above the spoiler (P1) shown in Figure 11a and 11c show good agreement between the two methodologies. Both plots show similar levels across the generation region, with the numerical results slightly underpredicting those resulting experimentally. Both signals decay along the Kolmogorov $f^{-5/3}$ energy decay slope along the high-frequency region. The difference in the 'smoothness' between the numerical

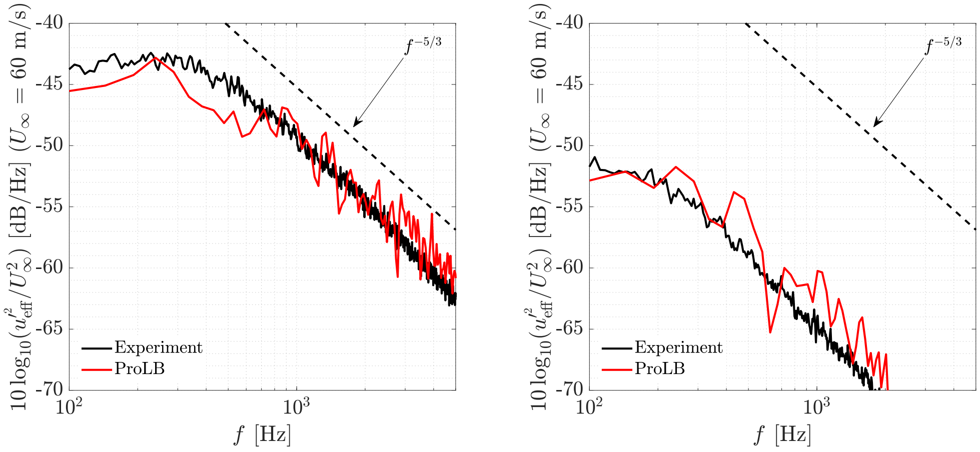

(a) Spectra at P_1 along acquisition plane HW_1 at x^* = 1.5.

(b) Spectra at P_2 along acquisition plane HW_1 at x^* = 1.5.

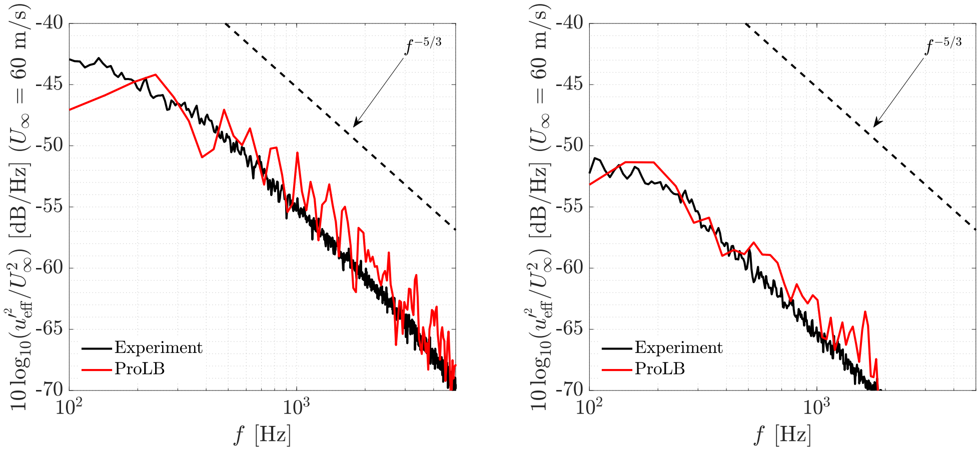

(c) Spectra at P_1 along acquisition plane HW_2 at x^* = 2.

(d) Spectra at P_2 along acquisition plane HW_2 at x^* = 2.

Fig. 11 Turbulent velocity spectra plots of $\mathbf{u}'_{\mathrm{eff}}$ at planes HW_1 and HW_2 measured at trailing edge and side-edge shear layers (shown in Fig. 3).

and experimental spectra is due to less averaging in the simulation data due to the smaller sampling time compared to the experimental results. When considering the turbulent spectra along the side-edge of the spoiler (P2) (shown in Fig. 11b and Fig. 11d), the two spectra analysed still show good agreement, albeit not as good as the position in the free shear layer above the spoiler (P1). In all cases, there is a slight underprediction at low frequencies.

2. Streamwise Planes - Velocity and Turbulence Intensity

The wake characteristics at different streamwise planes downstream of the spoiler were assessed for both the effective cooling velocity, U_{eff} and the turbulence intensity, $u'_{\mathrm{eff}}/U_\infty$ based on the fluctuations of the streamwise effective cooling velocity U_{eff}. Wake mapping was done along acquisition planes HW_1 at x^* = 1.5 and HW_2 at x^* = 2 and is shown in Fig. 12 and Fig. 13.

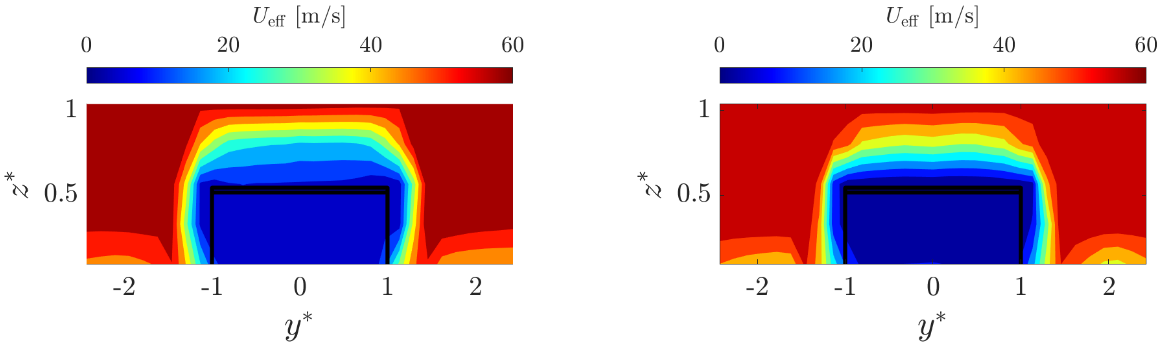

(a) Single Probe Hotwire: Velocity Mapping.

(b) ProLB: Velocity Mapping.

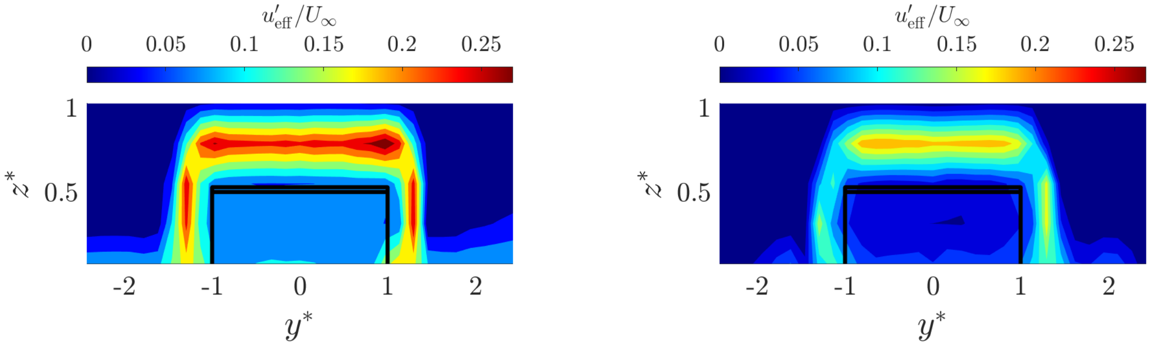

(c) Single Probe Hotwire: Turbulent Intensity Mapping.

(d) ProLB: Turbulent Intensity Mapping.

Fig. 12 Contour plots of the magnitude of $\mathbf{U_{eff}}$ and $\mathbf{u'_{eff}/U_\infty}$ at a streamwise location of $\mathbf{x^* = 1.5}$ (plane $\mathbf{HW_1}$). N.B. The double line outlines the finite thickness of the trailing edge of the spoiler.

Good agreement is observed with respect to U_{eff} maps along the two acquisition planes analysed. The wake topology convecting downstream shows a region of velocity deficit dominated by the bluff body recirculation vortex and growing free shear layers along the spoiler's free edges. Traces of velocity deficit due to the horseshoe vortices (discussed later) are observed centred around $y^* = \pm 2$.

Similarly, the turbulence intensity maps shown in Fig. 12c and 12d, and Fig. 13c and 13d show that the highest level of velocity fluctuations is observed along the shear layers generated from the trailing edge of the spoiler. The turbulence intensity is observed to decay as the wake convects downstream from the tailing edge. Comparing the numerical and experimental results, the numerical simulations underpredict the turbulence levels obtained experimentally. It was previously seen in single probe spectra that the numerical simulations underestimated some of the low-frequency content of the signal, whilst the agreement improved at higher frequencies.

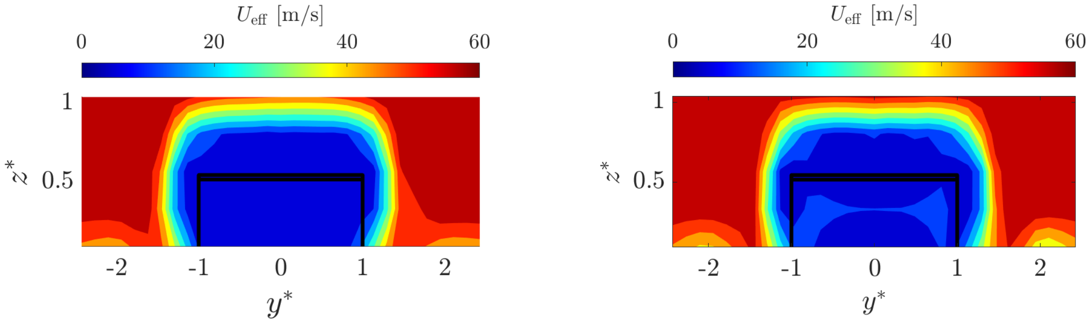

(a) Single probe Hotwire: Velocity Mapping.

(b) ProLB: Velocity Mapping.

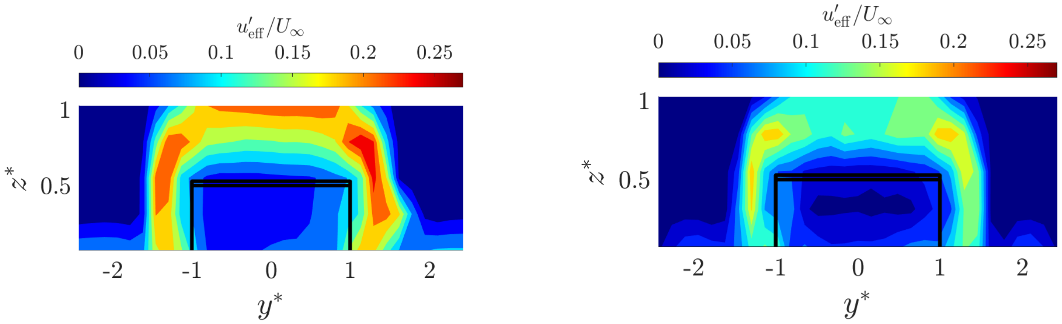

(c) Single Probe Hotwire: Turbulent Intensity Mapping.

(d) ProLB: Turbulent Intensity Mapping.

Fig. 13 Contour plots of the magnitude of U_{eff} and u'_{eff}/U_∞ at a streamwise location of x^* = 2 (plane HW_2). N.B. The double line outlines the finite thickness of the trailing edge of the spoiler.

3. Centre Span Plane - Velocity and 2D Turbulent Kinetic Energy

Two-dimensional, time-averaged PIV was used to validate the streamwise wake characteristics in the centre span plane (y= 0 m) downstream of the spoiler's trailing edge.

The mean velocity flow field comparison shown in Fig. 14 shows good agreement between experimental and numerical results. The wake is dominated by a bluff body recirculation region and a growing shear layer which grows as it convects downstream. Quiescent flow from underneath the base plate is observed to emanate upwards along the trailing edge of the base plate towards the trailing edge of the spoiler. This is due to the difference in pressure between the atmospheric pressure in the quiescent flow region underneath the baseplate and the low pressure within the wake. This emanating flow is further observed to bind the recirculation vortex, in turn forming an extended bluff body recirculation vortex bubble, which terminates at the trailing edge of the baseplate at x^* = 1.9. Both methodologies predict the recirculation vortex core at x^* = 1.4. However, ProLB slightly overpredicts the size of the recirculation vortex region. In ProLB, flow velocity emanating from underneath the baseplate is overpredicted, resulting in the formation of

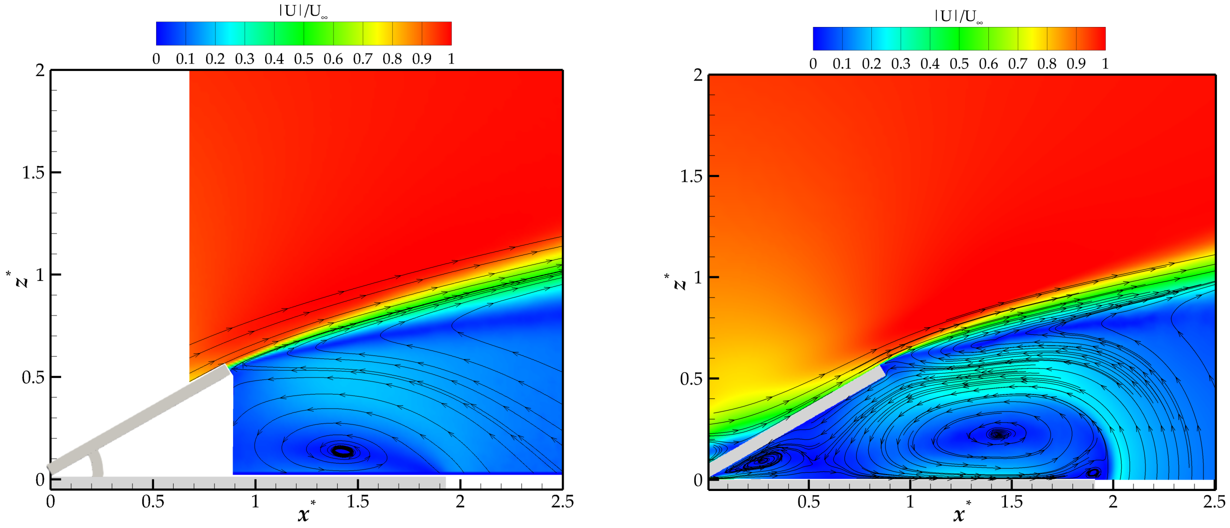

(a) MonoPIV

(b) ProLB

Fig. 14 Normalised mean velocity magnitude $|U|/U_\infty$ on the streamwise symmetry plane at y = 0 m.

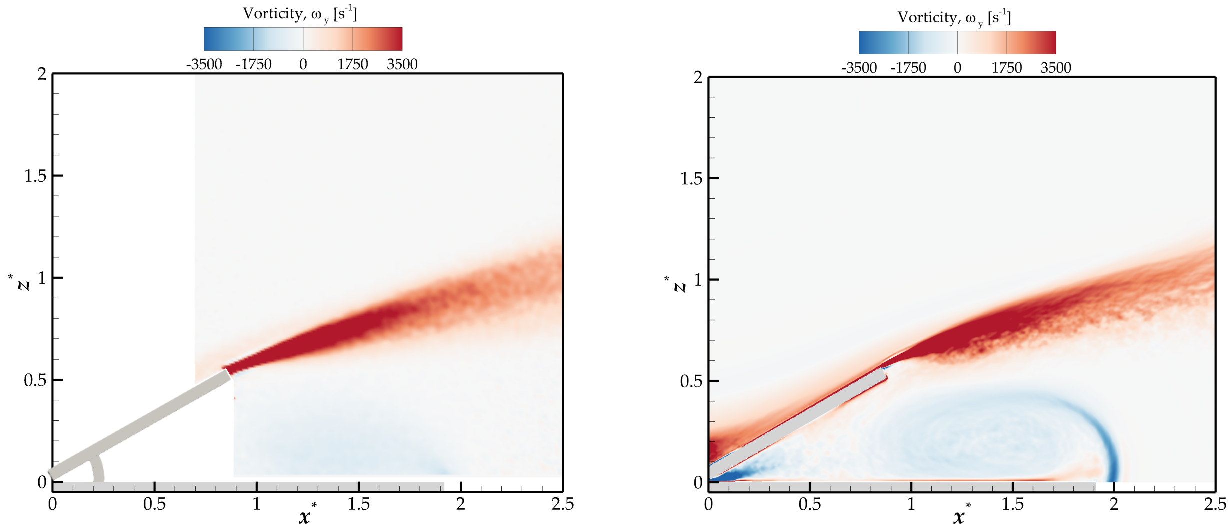

(a) MonoPIV

(b) ProLB

Fig. 15 Vorticity about the y-axis, ω_y on the streamwise symmetry plane at y = 0 m.

a larger recirculation region downstream of the spoiler.

The difference in the predicted vorticity component ω_y for both methodologies is shown in Fig. 15. The increase in velocity from underneath the baseplate results in higher levels of vorticity that result in a slight overprediction of the wake growth towards the trailing edge of the baseplate.

The subtle differences between the quiescent conditions underneath the model in the simulation may explain the overprediction of the convecting flow velocity between the two emanating flows from the trailing edge of the base plate. Despite modelling the fluid domain to mirror the dimensions of the anechoic wind tunnel and the model configuration, the precise spacing between the model and the floor, along with the inclusion of the false floor and acoustic wedges in the anechoic chamber, and the physical presence of the collector was not accounted for in the simulation. While necessary in to simulation to keep the mesh sizes reasonable and to simplify the specification of the boundary conditions, these simplifications may affect the flow underneath the base mounting plate and consequently influence the flow emanating from the trailing edge of the base mounting plate towards the trailing edge of the spoiler.

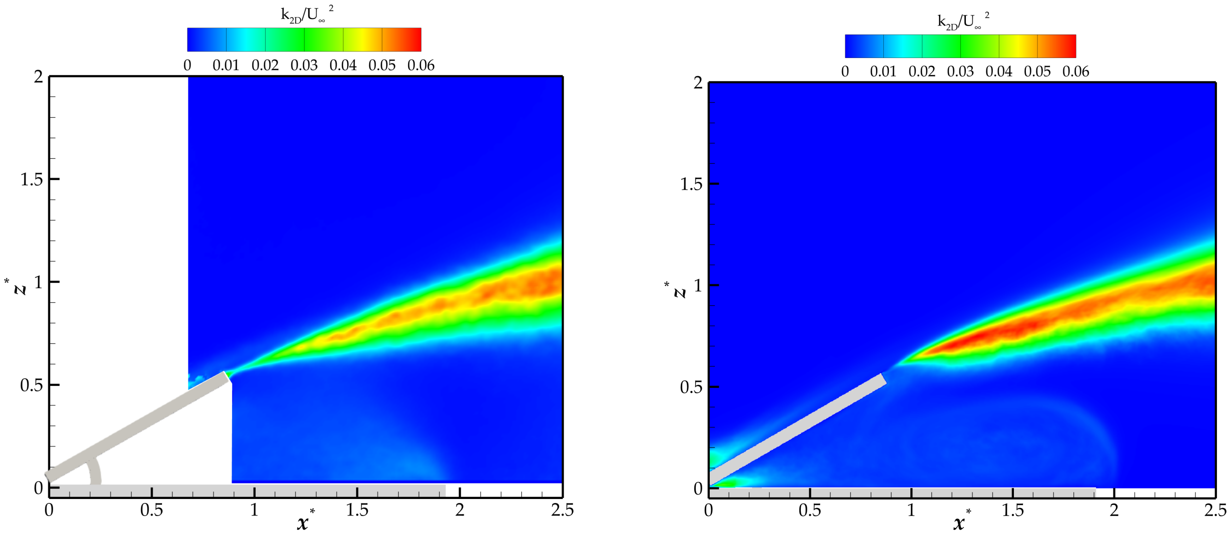

(a) MonoPIV

(b) ProLB

Fig. 16 Normalised two dimensional TKE, $\mathbf{k_{2D}/U_\infty^2}$ on the streamwise symmetry plane at y = 0 m.

Figure 16 shows the difference in the normalised two-dimensional turbulent kinetic energy ($k_{2\mathrm{D}}$) (defined in Eq. 6) based on the velocity fluctuations along the streamwise (u'_{x}) and vertical (u'_{z}) directions. The 2D turbulent kinetic energy is normalised with the square of the freestream velocity, U_∞^2. Agreement between the two methodologies is observed along the free shear layer generated from the horizontal trailing edge of the inclined spoiler.

$$k_{2\mathrm{D}} = \frac{1}{2}(\overline{u'_{\mathrm{x}}}^2 + \overline{u'_{\mathrm{z}}}^2) \ , \tag{6}$$

The wake expansion downstream of the inclined spoiler's trailing edge was validated against experimental results, as shown in Fig. 17. The wake edge at a given downstream location was identified as the point where the velocity profile reaches 99% of the asymptotic edge velocity outside of the shear layer. Both profiles exhibit an expanding wake convecting downstream of the spoiler due to fluid entrainment from the freestream, analogous to flow topologies observed for surface-mounted tabs. The wake height growth rate for each methodology was quantified using the wake height growth factor, k^*, defined in Eq. 7. The growth rates observed in both methodologies were similar, indicating good agreement in wake expansion rates between the two approaches.

$$k^* = \frac{\Delta z^*}{\Delta x^*} \quad , \tag{7}$$

where z^* represents the normalised vertical wake growth and x^* denotes the normalised downstream distance as a function of the chord on the spoiler.

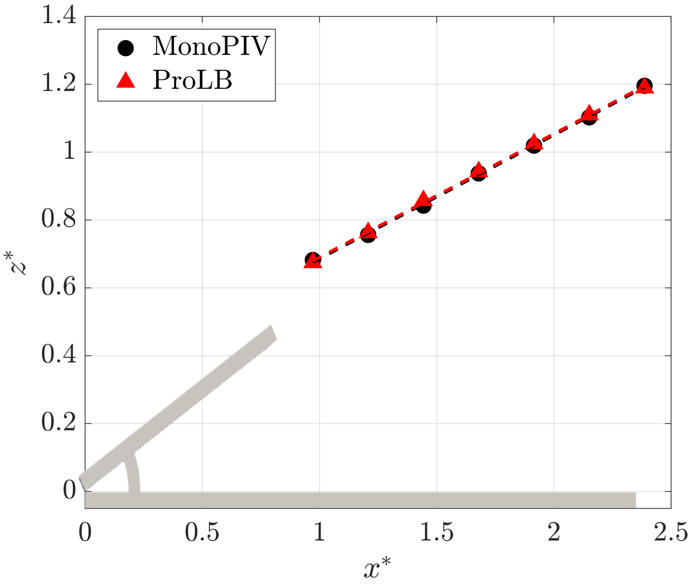

Fig. 17 Wake growth rate comparison between experimental and numerical results. The linear regression lines are indicated by dashed lines.

V. Flow Topology of a Deflected Spoiler at 30°

In the previous section, an experimental database for numerical validation was introduced, and a comparison was made to the Lattice Boltzmann code, ProLB. In spite of the relative simplicity of the geometries involved, there were several challenging flow phenomena to numerically capture accurately. In this section, the numerical results presented previously in the validation results are used to provide further insight into the flow topology around the inclined spoiler plate and the noise sources.

The flow topology around the inclined plate deflected at a deflection angle of 30° is shown in the Q-criterion iso-volume in Fig. 18a. The values of Q criterion were selected to highlight the discrete vortical structures associated with noise generation mechanisms around the wall-mounted plate. Similar to what is observed in the presence of junction flow [17, 18], the presence of the wall-mounted plate generates an adverse pressure gradient upstream of the plate. This causes the incoming boundary layer to separate upstream of the hinge of the plate, forming a horseshoe vortex structure, which is observed to continue downstream around the side-edges of the spoiler up to the trailing edge of the base mounting plate. Here, it mixes with the separated bluff body wake generated by the inclined spoiler plate.

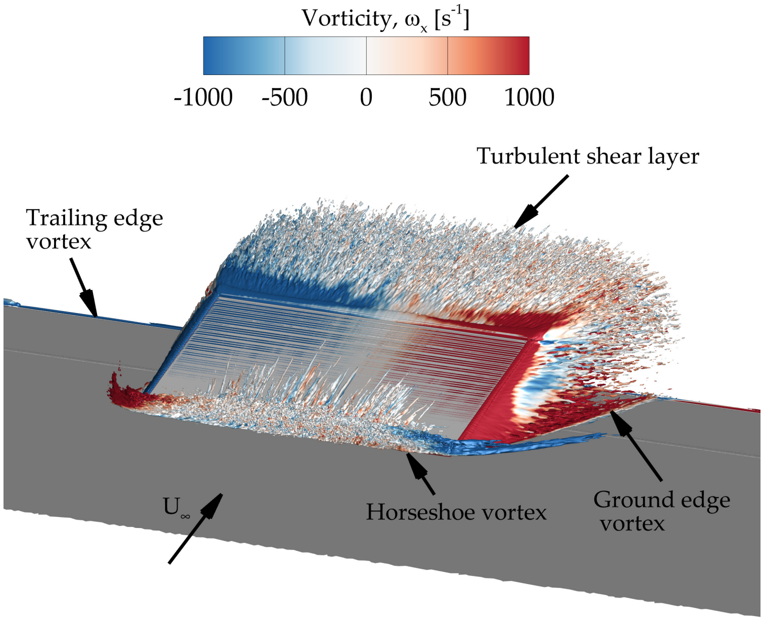

(a) Q-Criterion iso-volume (Q = 2.8×10^5) of the flow topology surrounding the inclined flat plate model. Contour filled with the vorticity about the x-axis, ω_x.

(b) Vorticity about the x-axis, ω_x plot along the spanwise $y-z$ plane at location $x^* = 1.5$ showing the formation of a ground edge vortices and horseshoe vortices.

Fig. 18 Flow topology highlighting the main vortical structures around the inclined flat spoiler model.

In addition to the horseshoe vortex originating from the separated flow upstream of the spoiler plate, another pair of ground-edge vortices originate from the inclined plate's leading edge. As highlighted in Fig. 18b, these vortices are observed to rotate in the opposite sense as the previously mentioned horseshoe vortices. Downstream of the spoiler, these are observed to stay attached along the mounting plate as they propagate downstream; hence, they are referred to here as ground edge vortices. As previously identified, there is a pressure gradient between the quiescent flow under the base plate and the low static pressure in the wake of the spoiler, causing the flow along the trailing edge of the base plate to convect upwards towards the spoiler. Due to the upwash generated by this flow, these ground vortices separate from the mounting plate at the trailing edge and convect upwards downstream of the trailing-edge. Downstream of the trailing-edge this upwash, combined with the upwash generated by the ground edge vortex pair, results in additional wake growth downstream of the base plate along the centreline ($y = 0$ m).

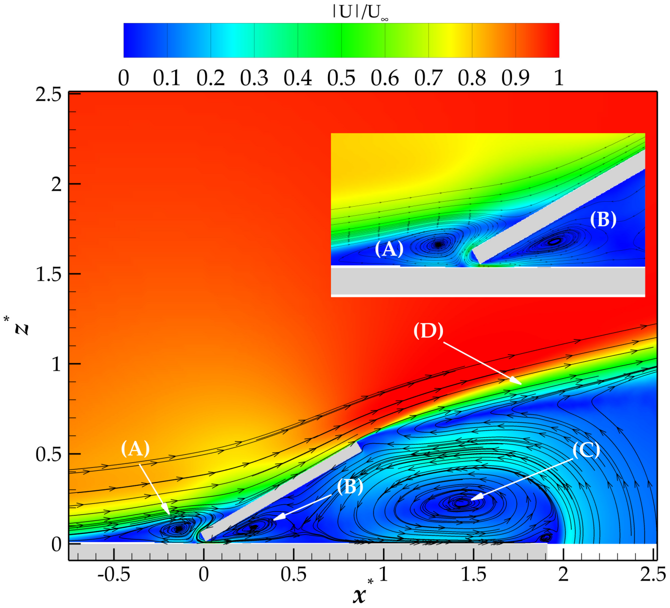

Fig. 19 Mean velocity contour and streamlines for a wall-mounted flat plate along the symmetry plane.

Figure 19 shows the mean flow field of the normalised velocity magnitude $|U|/U_\infty$ along the streamwise symmetry plane of the model at $y = 0$ m. Streamlines have been added to aid in visualising the location of the main recirculation regions in this plane. The important flow features are highlighted in the figure. Zone (A) highlights the upstream separation forming as a result of the boundary layer separation due to the adverse pressure gradient caused by the presence of the deflected plate. The flow is observed to separate upstream and attach shortly after the leading edge of the inclined plate. It is this separation and subsequent recirculation bubble that causes the drop in static pressure discussed previously in the on-surface pressure distributions upstream of the spoiler hinge.

Additionally, flow is observed emanating through the hinge gap between the leading edge of the inclined plate and the base plate due to the pressure difference between the upstream and downstream regions of the base plate. This gap is well immersed in the boundary layer; hence, the entertainment velocity through the gap is much lower than the freestream velocity. The flow through the hinge results in the formation of a small recirculation region (B) immediately downstream of the hinge, which is observed to attach to the downstream face of the spoiler.

Zone (C) highlights the bluff body recirculation region downstream of the spoiler plate. As discussed in the validation section, the bluff body recirculation region's size is dictated by the length of the base plate downstream of the model. Flow emanating from the quiescent flow beneath the trailing edge of the base plate is convected towards the spoiler due to the pressure gradients, bounding the recirculation bubble forming downstream of the spoiler. The bulk wake is bounded by a shear layer (D) generated by the separation occurring along the trailing edge of the spoiler. The wake is observed to grow as it convects downstream. This is highlighted in Fig. 20a and Fig. 20b showing the wake profile downstream of the spoiler for both the normalised velocity magnitude and the normalised three-dimensional turbulent kinetic energy.

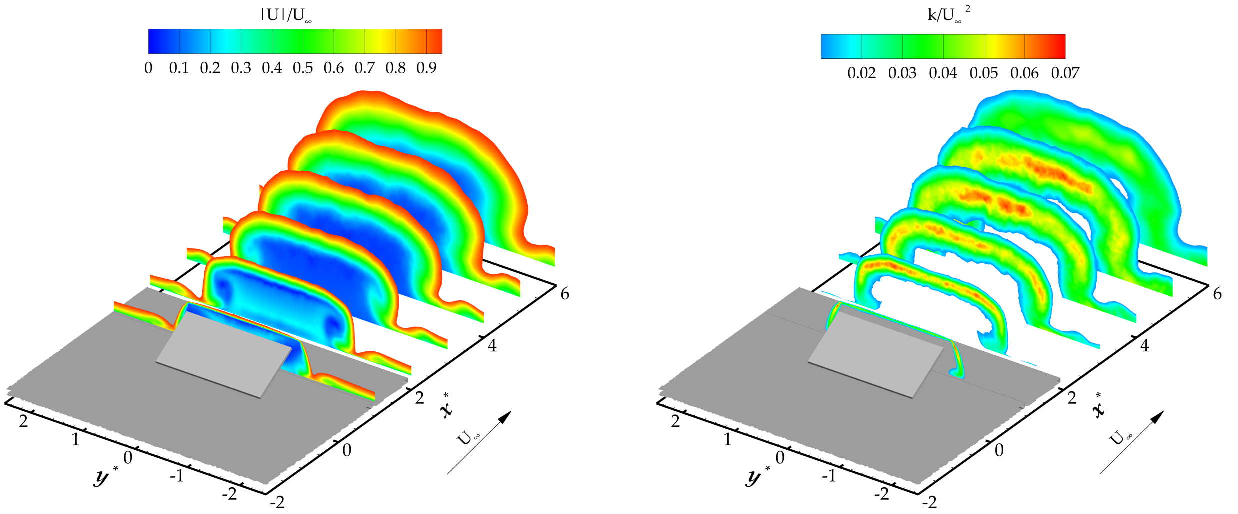

(a) Normalised mean flow field of the velocity magnitude downstream of the inclined spoiler.

(b) Normalised three-dimensional turbulent kinetic energy downstream of the spoiler.

Fig. 20 Time-averaged flow field characteristics downstream of the wall-mounted inclined spoiler.

VI. Noise Source Characterisation

The flow topology for a wall-mounted deflected spoiler is observed to be defined by a broadband turbulent wake dominated by an unsteady shear layer generated from the trailing edge of the spoiler, an upstream separation which results in a horseshoe vortex, and a pair of ground edge vortices which are observed to stay attached to the base mounting plate until the trailing-edge of the mounting plate. The next step is to understand which of these different flow features are responsible for the noise generation of this configuration.

A band-filtered on-surface pressure analysis was calculated using the solid FW-H surfaces at different frequencies. Figure 21a shows the unsteady fluctuations of the on-surface pressures integrated over a frequency range with a one-third centre frequency of 2.0 kHz. At this frequency, the noise generated by the spoiler plate alone is close to its peak value as shown in Fig. 10. As previously discussed, the baseplate contributed more at lower frequencies. Two primary regions of high pressure fluctuations were determined. The first was the horseshoe vortex that formed upstream of the hinge.

The highest pressure fluctuations occurred on the upstream part. Once the horseshoe vortex wrapped around the side of the spoiler, the fluctuations were diminished. The second region corresponded to the location of the ground edge vortices. Other lesser regions were the free side-edges and trailing edge of the spoiler, as well as the upstream face, where unsteady flow was generated by the separated flow upstream of the spoiler hinge impinged on the upstream face of the spoiler. Similar results are seen at 8 kHz (Figure 21c). At this frequency, the pressure fluctuations associated with the ground edge vortices dominated.

To see if and how these on-surface pressure fluctuations radiated as sound, the on-surface band-filtered pressure contours were compared to three-dimensional beamforming results obtained from the numerical simulations. Further details of the methodology are included in Appendix B. The results for a one-third octave frequency of 2 kHz (wavelength λ = 0.170 m), shown in Fig. 21a and Fig. 21b, show that the ground edge vortices and the spoiler side-edges are the prominent sources. There is still a source associated with the horseshoe vortex, but it is smaller in strength. At 8 kHz (wavelength λ = 0.043 m), shown in Fig. 21c and Fig. 21d, the sources are similar. Due to the smaller wavelength, the sources are more localised. There is a clear source along the horseshoe vortex upstream of the spoiler hinge. The ground edge vortices forming at the side-edge of the spoiler are the most significant source in the 3D beamforming.

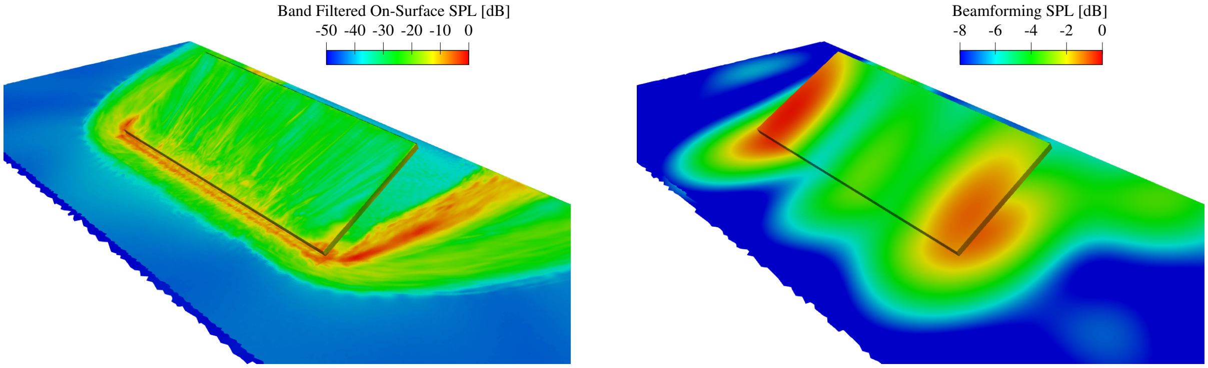

(a) f = 2 kHz - Band filtered on-surface pressure fluctuations.

(b) f = 2 kHz - Three dimensional numerical beamforming source map.

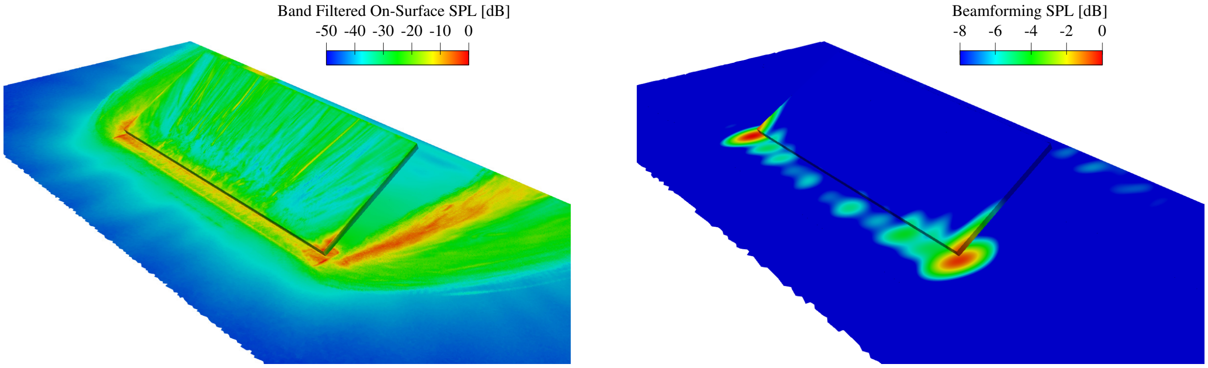

(c) f = 8 kHz - Band filtered on-surface pressure fluctuations.

(d) f = 8 kHz - Three dimensional numerical beamforming source map.

Fig. 21 Comparison between band filtered on-surface pressures (left) and three dimensional numerical beamforming source maps (right) for different one-third octave band centre frequencies.

VII. Conclusions

In this paper, an experimental validation database for a spoiler mounted to a flat plate was described. The experimental database consisted of forces, on-surface pressure measurements, hotwire measurements, particle image velocimetry measurements and total pressure rake measurements for boundary layer profiles. The motivation behind mounting the spoiler to a flat plate was to decouple its sources from changes in the other high-lift wing sources when the spoiler is deflected. The spoiler was deflected at an angle of 30°. This work presents a comprehensive aerodynamic and acoustic experimental database for numerical validation. It also links the noise sources to the flow topology features responsible for these noise sources.

Results from numerical simulations performed using the Lattice Boltzmann code ProLB were compared to the experimental validation database for this case. In spite of the relatively simple geometries involved in this test case, it was still quite a challenging case to accurately simulate. In particular, the upstream separation bubble, which ultimately formed the horseshoe vortex around the spoiler, was difficult to predict in the correct location upstream of the spoiler hinge line. The aerodynamic drag force was predicted within 5.4% of the experimental results. The on-surface pressure distributions explained this small discrepancy. While the base pressure on the downstream face of the spoiler was well predicted, the small discrepancies in the upstream separation bubble location and subsequent reattachment, resulted in small differences in the pressures on the upstream face of the spoiler.

The wake characteristics, mean velocities, turbulent intensities and 2D turbulent kinetic energy, were determined from hotwire anemometry and particle image velocity. The numerical simulation showed good agreement with the experimental data. There was some difference in the interaction with the wake of the spoiler and the quiescent flow underneath the base plate, resulting in a slight overestimation of the base recirculation region. Also, the turbulent spectra showed a slight underprediction at low frequencies resulting in a slight underprediction in the turbulent intensity measured in the wake.

The acoustic predictions were presented at three different polar angles. There was excellent agreement above 630 Hz with the porous FWH prediction. However, at low frequencies, there was an underprediction. The reason for this was explored using the solid FWH prediction with each of the solid surfaces. It was shown that at low frequencies, it is the contribution from the pressure fluctuations on the mounting base plate, caused by the spoiler wake, that dominates. The porous FWH surface only contains a part of the baseplate and therefore misses some of the low frequency noise. While the solid FWH recovers the low frequency noise (particularly upstream and overhead), it overpredicts the noise at frequencies above 1 kHz compared to the porous FWH prediction.

Using the validated numerical results, the flow topology of the deflected spoiler was described. It consisted of three main flow features. The first was a separation bubble upstream of the spoiler hinge resulting in a horseshoe vortex that wrapped around the sides of the spoiler. The second was ground edge vortices which were attached to the base plate up to the trailing-edge. These ground edge vortices rotated in the opposite sense to the horseshoe vortex on each side. The third was an arch-type broadband wake downstream of the spoiler that was symmetric about the center span of the spoiler. The wake was characterised by an absence of coherent vortex shedding due to the mounting plate inhibiting the formation of a shear layer of opposite sign vorticity on the lower edge of the plate.

To investigate the acoustic sources on this configuration, a combination of band-filtered on-surface pressures and 3D numerical beamforming was used. Two primary regions of high pressure fluctuations were determined. The first was the horseshoe vortex that formed upstream of the hinge particular upstream of the spoiler hinge. The second region corresponded to the location of the ground edge vortices. There were also fluctuations corresponding to the broadband wake. The highest fluctuations were close to the spoiler side-edges. The 3D beamforming showed that the acoustic source associated with the ground edge vortices and the spoiler side-edges were the dominant acoustic sources in this configuration, particularly as the frequency increased.

Appendix A

Microphone	Polar Angle	x (m)	y (m)	z (m)
1	Overhead 70°	-0.631	0	1.335
2	Overhead 76°	-0.421	0	1.333
3	Overhead 83°	-0.211	0	1.331
4	Overhead 90°	0	0	1.331
5	Overhead 94°	0.114	0	1.330
6	Overhead 97°	0.226	0	1.330
7	Overhead 101°	0.336	0	1.330

Table A.1 Microphone locations with respect to the model axis shown in Fig. 1.

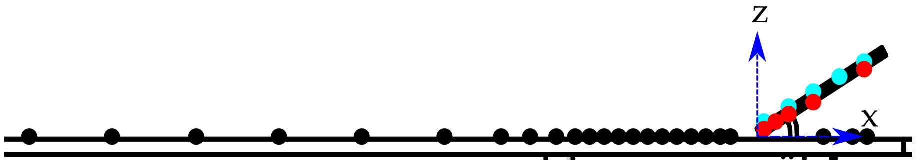

Fig. A.1 Schematic of the location of the static pressure taps on the model. • Base mounting plate; • Spoiler's upstream face; • Spoiler's downstream face.

Pressure Tap No.	Location	x (m)	y (m)	z (m)
1	Base Mounting Plate	-0.497	0	0
2	Base Mounting Plate	-0.440	0	0
3	Base Mounting Plate	-0.382	0	0
4	Base Mounting Plate	-0.325	0	0
5	Base Mounting Plate	-0.268	0	0
6	Base Mounting Plate	-0.211	0	0
7	Base Mounting Plate	-0.172	0	0
8	Base Mounting Plate	-0.152	0	0
9	Base Mounting Plate	-0.134	0	0
10	Base Mounting Plate	-0.121	0	0
11	Base Mounting Plate	-0.111	0	0
12	Base Mounting Plate	-0.101	0	0
13	Base Mounting Plate	-0.091	0	0
14	Base Mounting Plate	-0.081	0	0
15	Base Mounting Plate	-0.071	0	0
16	Base Mounting Plate	-0.061	0	0
17	Base Mounting Plate	-0.051	0	0
18	Base Mounting Plate	-0.041	0	0
19	Base Mounting Plate	-0.031	0	0
20	Base Mounting Plate	-0.021	0	0
21	Base Mounting Plate	-0.014	0	0
22	Base Mounting Plate	0.050	0	0
23	Base Mounting Plate	0.070	0	0
24	Base Mounting Plate	0.080	0	0
25	Spoiler’s Upstream Face	0.009	0	0.010
26	Spoiler’s Upstream Face	0.026	0	0.020
27	Spoiler’s Upstream Face	0.043	0	0.030
28	Spoiler’s Upstream Face	0.061	0	0.040
29	Spoiler’s Upstream Face	0.078	0	0.050
30	Spoiler’s Downstream Face	0.009	0	0.005
31	Spoiler’s Downstream Face	0.017	0	0.01
32	Spoiler’s Downstream Face	0.026	0	0.015
33	Spoiler’s Downstream Face	0.039	0	0.023
34	Spoiler’s Downstream Face	0.078	0	0.045

Table A.2 Pressure tap positions on the symmetry plane. The coordinate system is shown in Fig. 1.

Acquisition Point Location	y (m)	z (m)
P_1	0	0.087
P_2	-0.125	0.054

Table A.3 Position of the single probe turbulent hotwire measurements with respect to the model axis shown in Fig. 1.

Coordinate Axis	Vector Limits (m)
x	$-0.147 \leq x \leq 0.194$
y	$-0.35 \leq y \leq 0.35$
z	$0 \leq z \leq 0.18$

Table A.4 Geometric definition of the porous FW-H surface used in the numerical simulations with respect to the model axis shown in Fig. 1.

Appendix B: Numerical 3D Beamforming

112 virtual microphones were placed on a box that surrounded the geometry. The microphones were placed on three faces of a box; the two side faces and the top face. The microphones were only placed above the mounting place with no microphones below it. The microphone distribution was an evenly distributed circular distribution on a cylinder that was then projected onto the three faces of the box coincident with the edges of the wind tunnel nozzle. Various different orientations and number of microphones were experimented with. The signals at each of the microphone locations were determined using the porous FW-H surface results.

The steps in the 3D numerical beamforming are first to compute the cross spectral matrix between all 112 microphones. The coordinates of the scan plane need to be defined. In this case the surface mesh from the numerical simulation is used to determine the scan plane points. This ensures that all sources determined by the 3D beamformer are coincident with the solid surfaces in the simulation. The use of the surface mesh from the simulation for the scan plane results in a large number of scan plane points ($O(10^6)$). However, this does not have too much of an influence on the calculation time since the computation time and memory requirements are primarily a function of the cross spectral matrix size, which scales with the number of microphones squared.

The beamforming is performed using a standard frequency domain beamformer. As opposed to delay and sum beamforming in the time domain, here the time delays are expressed as phase shifts calculated from the cross spectral matrix.

The output of the beamformer (the estimate for the true mean square source strength) is given by,

$$Q_{\mathrm{opt}} = \frac{\mathbf{g}^{\dagger}\mathbf{S}_{pp}\,\mathbf{g}}{[\mathbf{g}^{\dagger}\mathbf{g}]^{2}} \quad , \tag{8}$$

where $\mathbf{S}_{pp}$ is the cross spectral matrix of the 112 microphones forming the 3D phased microphone array. In this case the cross spectral matrix was averaged over 6 blocks of data with an FFT size of 1024 and a sampling frequency of 98 kHz. The total signal length was 0.1 s. These are very short signal lengths compared to those typically acquired in experimental beamforming. However, the numerical data contains much less noise than in an experiment.

The steering vector **g** used in this beamformer for each point on the scan plane is defined as follows,

$$\mathbf{g}(\mathbf{x}, \mathbf{y}, \omega) = \frac{\mathrm{i}\omega\rho_0\,\mathrm{e}^{\mathrm{i}\omega\sigma}}{4\pi R} \quad , \tag{9}$$

where **x** represents the microphone locations, **y** represents the scan plane locations, ω represents the frequency and the subscript 0 represents the freestream value. In this definition of the steering vector, it assumes a monopole point source at each location on the scan plane and spherical spreading from the scan plane to the microphone locations.

These assumptions are the same that are made routinely when using conventional frequency domain beamforming on experimental data in wind tunnels. In this work, the 3D beamforming is only used to determine which sources determined through band-filtered on-surface pressures actually propagate to the farfield, and not to provide absolute source levels.

The effective propagation distance between the microphones and the scan plane is defined as,

$$R = \sqrt{\left(\mathbf{M} \cdot (\mathbf{x} - \mathbf{y})\right)^2 + \beta^2 ||\mathbf{x} - \mathbf{y}||^2} \ , \tag{10}$$

where $\beta = \sqrt{1 - ||\mathbf{M}||^2}$ and $\mathbf{M}$ is the Mach number vector. This expression for the effective propagation distance accounts for the mean flow effects in a uniform flow.

The time delay is expressed as,

$$\sigma = \frac{1}{c_0} \frac{R - \left(\mathbf{M} \cdot (\mathbf{x} - \mathbf{y}_0)\right)}{\beta^2} \ , \tag{11}$$

where c_0 is the speed of sound.

In the 3D numerical beamforming performed here, the diagonal of the CSM is not removed as is typically done in experimental measurements. The CSM is typically removed in experiments as the noise arising from either the turbulent boundary layer in contact with a flush-mounted microphone or wind tunnel background noise in the facility reduces the performance of the phased microphone array. These noise sources can be assumed to be uncorrelated over the array microphones, and one can therefore expect that in the CSM this noise will average to zero except on the leading diagonal, hence its removal. In the numerical simulations this is less of an issue and therefore the diagonal is retained in the CSM. Finally, the beamforming outputs are integrated over the relevant one-third octave band presented.

Acknowledgements

This work was sponsored in part by the research project INnoVative dEsign of iNstalled airframe componenTs for aircraft nOise Reduction (INVENTOR), which has received funding from the European Union's Horizon 2020 research and innovation program under grant agreement No. 860538.

All LaBS/ProLB numerical simulations have been carried out on Airbus' HPC resources using LaBS 2.6.3 DC.

The authors would like to thank Dr Yolanda Hou for her help with the three-dimensional numerical beamforming cases.

Data published in this paper are available from the University of Southampton repository at https://doi.org/10.5258/SOTON/D3189

References

[1] Filippone, A., "Steep-descent maneuver of transport aircraft," *Journal of Aircraft*, Vol. 44, No. 5, 2007, pp. 1727–1739. https://doi.org/10.2514/1.28980.

[2] Antoine, N., and Kroo, I., "Aircraft optimization for minimal environmental impact," *Journal of Aircraft*, Vol. 41, No. 4, 2004, pp. 790–797. https://doi.org/10.2514/1.71.

[3] Mertol, B., "An Airbrake Design Methodology for Steep Approaches," *New Results in Numerical and Experimental Fluid Mechanics VI*, Springer Berlin Heidelberg, 2008, pp. 1–8. https://doi.org/10.1007/978-3-540-74460-3_1.

[4] Dobrzynski, W., "Almost 40 years of airframe noise research: What did we achieve?" *Journal of Aircraft*, Vol. 47, No. 2, 2010, pp. 353–367. https://doi.org/10.2514/1.44457.

[5] Ayoub, A., Satynarayana, B., Karamcheti, K., and Seetharam, H., "Unsteady flow patterns associated with spoiler control devices," *20th Aerospace Sciences Meeting, AIAA Paper 1982-127*, 1982. https://doi.org/10.2514/6.1982-127.

[6] McLachlan, B., Karamecheti, K., Ayoub, A., and Hadjidakis, G., "A study of the unsteady flow field of an airfoil with deflected spoiler," *10th Atmospheric Flight Mechanic Conference, AIAA Paper 1983-2131*, 1983. https://doi.org/10.2514/6.1983-2131.

[7] Kanjere, K., Zhang, X., Hu, Z., and Angland, D., "Aeroacoustic Investigation of Deployed Spoiler during Steep Approach Landing," *16th AIAA/CEAS Aeroacoustics Conference, AIAA Paper 2010-3992*, 2010. https://doi.org/10.2514/6.2010-3992.

[8] Good, M. C., and Joubert, P. N., "The form drag of two-dimensional bluff-plates immersed in turbulent boundary layers," *Journal of Fluid Mechanics*, Vol. 31, No. 3, 1968, pp. 547–582. https://doi.org/10.1017/S0022112068000327.

[9] Okamoto, S., "Experimental Investigation of Flow Past Bluff Body of Square Section Placed on Ground Plane," *Bulletin of JSME*, Vol. 28, No. 239, 1985, pp. 815–823. https://doi.org/10.1299/jsme1958.28.815.

[10] Arie, M., and Rouse, H., "Experiments on two-dimensional flow over a normal wall," *Journal of Fluid Mechanics*, Vol. 1, No. 2, 1956, pp. 129–141. https://doi.org/10.1017/S0022112056000093.

[11] Montes Gomez, E., and Sumner, D., "The wake of a rectangular flat plate," *Fluid Dynamics Research*, Vol. 54, No. 6, 2022, pp. 0–23. https://doi.org/10.1088/1873-7005/acabe3.

[12] Hosseini, Z., Bourgeois, J. A., and Martinuzzi, R. J., "Large-scale structures in dipole and quadrupole wakes of a wall-mounted finite rectangular cylinder," *Experiments in Fluids*, Vol. 54, No. 9, 2013, pp. 1–16. https://doi.org/10.1007/s00348-013-1595-2.

[13] Sumner, D., Heseltine, J. L., and Dansereau, O. J. P., "Wake structure of a finite circular cylinder of small aspect ratio," *Experiments in Fluids*, Vol. 37, No. 5, 2004, pp. 720–730. https://doi.org/10.1007/s00348-004-0862-7.

[14] Martinuzzi, R., and Tropea, C., "The Flow Around Surface-Mounted, Prismatic Obstacles Placed in a Fully Developed Channel Flow (Data Bank Contribution*)," *Journal of Fluid Engineering*, Vol. 115, 1993, pp. 85–92. https://doi.org/10.1115/1.2910118.

[15] Martinuzzi, R. J., "Dual vortex structure shedding from low aspect ratio, surface-mounted pyramids," *Journal of Turbulence*, Vol. 9, 2008, pp. 1–16. https://doi.org/10.1080/14685240802272117.

[16] Wang, H. F., and Zhou, Y., "The finite-length square cylinder near wake," *Journal of Fluid Mechanics*, Vol. 638, 2009, pp. 453–490. https://doi.org/10.1017/S0022112009990693.

[17] Doligalski, T. L., Smith, C. R., and Walker, J. D., "Vortex interactions with walls," *Annual Review of Fluid Mechanics*, Vol. 26, No. 1, 1994, pp. 573–616. https://doi.org/10.1146/annurev.fl.26.010194.003041.

[18] Devenport, W. J., and Simpson, R. L., "Time-dependent and time-averaged turbulence structure near the nose of a wing-body junction," *Journal of Fluid Mechanics*, Vol. 210, No. 23, 1990, pp. 23–55. https://doi.org/10.1017/S0022112090001215.

[19] Everitt, K. W., "Normal Flat Plate Close To a Large Plane Surface." *Aeronautical Quarterly*, Vol. 33, No. pt 1, 1982, pp. 90–104. https://doi.org/10.1017/s0001925900009318.

[20] Sakamoto, H., and Arie, M., "Flow Around a Normal Plate of Finite Width Immersed in a Turbulent Boundary Layer." *Journal of Fluids Engineering*, Vol. 105, No. 1, 1983, pp. 98–104. https://doi.org/10.1115/1.3240950, URL https://doi.org/10.1115/1.3240950.

[21] Sakamoto, H., H; Haniu, "Arch-type Vortex Formed Behind a Normal Plate Placed in a Laminar Boundary Layer," *Bulletin of JSME*, Vol. 29, No. 255, 1986, pp. 2857–2862. https://doi.org/10.1299/jsme1958.29.2857.

[22] Gretta, W. J., and Smith, C. R., "The flow structure and statistics of a passive mixing tab," *Journal of Fluids Engineering*, Vol. 115, 1993, pp. 255–263. https://doi.org/10.1115/1.2910133, URL https://doi.org/10.1115/1.2910133.

[23] Dong, S., and Meng, H., "Flow past a trapezoidal tab," *Journal of Fluid Mechanics*, Vol. 510, No. 1, 2004, pp. 219–242. https://doi.org/10.1017/S0022112004009486.

[24] Hamed, A. M., Pagan-Vazquez, A., Khovalyg, D., Zhang, Z., and Chamorro, L. P., "Vortical structures in the near wake of tabs with various geometries," *Journal of Fluid Mechanics*, Vol. 825, 2017, pp. 167–188. https://doi.org/10.1017/jfm.2017.384.

[25] Becker, S., Hahn, C., Kaltenbacher, M., and Lerch, R., "Flow-induced sound of wall-mounted cylinders with different geometries," *AIAA Journal*, Vol. 46, No. 9, 2008, pp. 2265–2281. https://doi.org/10.2514/1.34865.

[26] King, W. F., and Pfizenmaier, E., "An experimental study of sound generated by flows around cylinders of different cross-section," *Journal of Sound and Vibration*, Vol. 328, No. 3, 2009, pp. 318–337. https://doi.org/10.1016/j.jsv.2009.07.034, URL http://dx.doi.org/10.1016/j.jsv.2009.07.034.

[27] Moreau, D. J., and Doolan, C. J., "Flow-induced sound of wall-mounted finite length cylinders," *AIAA Journal*, Vol. 51, No. 10, 2013, pp. 2493–2502. https://doi.org/10.2514/1.J052391.

[28] Porteous, R., Moreau, D. J., and Doolan, C. J., "A review of flow-induced noise from finite wall-mounted cylinders," *Journal of Fluids and Structures*, Vol. 51, 2014, pp. 240–254. https://doi.org/10.1016/j.jfluidstructs.2014.08.012, URL http://dx.doi.org/10.1016/j.jfluidstructs.2014.08.012.

[29] Parnis, O., and Angland, D., "Effect of Deflection Angle on the Noise and Aerodynamic Loads Generated by a Wall-Mounted Flat Plate," *AIAA Aviation 2023 Forum, AIAA Paper 2023-3493*, 2023. https://doi.org/10.2514/6.2023-3493.

[30] Ivanova, Z., and Angland, D., "Southampton Anechoic Wind Tunnel (SotonAWT) Aerodynamic and Acoustic Characterisation," *28th AIAA/CEAS Aeroacoustics 2022 Conference, AIAA Paper 2022-2854*, 2022. https://doi.org/10.2514/6.2022-2854.

[31] JCGM, *Evaluation of measurement data — Guide to the expression of uncertainty in measurement*, Sèvres, France, 2008. URL http://www.bipm.org/en/committees/jc/jcgm, first edition, corrected version 2010.

[32] Leveque, E., Touil, H., Malik, S., Ricot, D., and Sengissen, A., "Wall-modeled large-eddy simulation of the flow past a rod-airfoil tandem by the Lattice Boltzmann method," *International Journal of Numerical Methods for Heat and Fluid Flow*, Vol. 28, No. 5, 2018, pp. 1096–1116. https://doi.org/10.1108/hff-06-2017-0258.

[33] Afzal, N., "Wake Layer in a Turbulent Boundary Layer with Pressure Gradient: A New Approach," *Fluid Mechanics and Its Applications IUTAM Symposium on Asymptotic Methods for Turbulent Shear Flows at High Reynolds Numbers*, , No. 1996, 1996, pp. 95–118. https://doi.org/10.1007/978-94-009-1728-6{_}9.

[34] Patel, V., and Sotiropoulos, F., "Longitudinal Curvature effects in turbulent boundary layers," *Progress in Aerospace Sciences*, Vol. 33, 1997, pp. 1–70. https://doi.org/10.1016/S0376-0421(96)00001-2.

[35] Farassat, F., and Succi, G., "A review of propeller discrete frequency noise prediction technology with emphasis on two current methods for time domain calculations." *Journal of Sound and Vibration*, Vol. 71, No. 3, 1980, pp. 399–419. https://doi.org/10.1016/0022-460X(80)90422-8.

[36] Jorgensen, F., "Directional sensitivity of wire and fibre-film probes. An experimental study." , 1971.

[37] Champagne, F., Sleicher, C., and O.H, W., "Turbulence measurements with inclined hot-wires. Part 1. Hear transfer experiments with inclined hot-wire." *Journal of Fluid Mechanics*, Vol. 28, No. 1, 1966, pp. 177–182. https://doi.org/10.1017/S0022112067001971.

[38] Jorgensen, F., "How to measure turbulence with hot-wire anemometers - a practical guide," Tech. rep., Dantec Dynamics, 2002.

[39] Tropea, C., Yarin, A., and Foss, J. (eds.), *Springer Handbook of Experimental Fluid Mechanics*, Vol. 5, Springer, 2007. https://doi.org/10.1007/978-3-540-30299-5.

[40] Welch, P., "The use of the Estimation of Power Sectra: A Method Based on Time Averaging Over Short, Modified Periodograms," *IEEE Transection on Audio and Electroacoustics*, Vol. 15, No. 2, 1967, pp. 70–73. https://doi.org/10.1109/TAU.1967.1161901.